

# 1 **Allosteric activation or inhibition of PI3K $\gamma$ mediated through** 2 **conformational changes in the p110 $\gamma$ helical domain**

3  
4 Noah J Harris<sup>1\*</sup>, Meredith L Jenkins<sup>1\*</sup>, Sung-Eun Nam<sup>2</sup> Manoj K Rathinaswamy<sup>1</sup>,  
5 Matthew AH Parson<sup>1</sup>, Harish Ranga-Prasad<sup>1</sup>, Udit Dalwadi<sup>2</sup>, Brandon E Moeller<sup>1</sup>,  
6 Eleanor Sheekey<sup>1</sup>, Scott D Hansen<sup>3</sup>, Calvin K Yip<sup>2%</sup>, and John E Burke<sup>1,2%</sup>

7  
8  
9 <sup>1</sup>Department of Biochemistry and Microbiology, University of Victoria, Victoria, British  
10 Columbia, V8W 2Y2, Canada

11 <sup>2</sup>Department of Biochemistry and Molecular Biology, The University of British Columbia,  
12 Vancouver, British Columbia V6T 1Z3, Canada

13 <sup>3</sup>Department of Chemistry and Biochemistry, Institute of Molecular Biology, University of  
14 Oregon, Eugene, OR 97403

15  
16 \*These authors contributed equally

17 <sup>%</sup>To whom correspondence should be addressed: John E. Burke

18 Tel: 1-250-721-8732, email: [jeburke@uvic.ca](mailto:jeburke@uvic.ca)

19 Calvin K. Yip

20 Tel: 1-604-827-3976, email: [calvin.yip@ubc.ca](mailto:calvin.yip@ubc.ca)

21  
22  
23 **Keywords:** PI3K, PIK3CG, PI3K $\gamma$ , p110 $\gamma$ , p101, p84, PIK3R5, PIK3R6,  
24 phosphoinositide 3-kinase, hydrogen exchange, protein kinase C, PKC, nanobodies.

30 **Abstract**

31 PI3K $\gamma$  is a critical immune signaling enzyme activated downstream of diverse cell  
32 surface molecules, including Ras, PKC $\beta$  activated by the IgE receptor, and G $\beta\gamma$  subunits  
33 released from activated GPCRs. PI3K $\gamma$  can form two distinct complexes, with the p110 $\gamma$   
34 catalytic subunit binding to either a p101 or p84 regulatory subunit, with these complexes  
35 being differentially activated by upstream stimuli. Here using a combination of Cryo  
36 electron microscopy, HDX-MS, and biochemical assays we have identified novel roles of  
37 the helical domain of p110 $\gamma$  in regulating lipid kinase activity of distinct PI3K $\gamma$  complexes.  
38 We defined the molecular basis for how an allosteric inhibitory nanobody potently inhibits  
39 kinase activity through rigidifying the helical domain and regulatory motif of the kinase  
40 domain. The nanobody did not block either p110 $\gamma$  membrane recruitment or Ras/G $\beta\gamma$   
41 binding, but instead decreased ATP turnover. We also identified that p110 $\gamma$  can be  
42 activated by dual PKC $\beta$  helical domain phosphorylation leading to partial unfolding of an  
43 N-terminal region of the helical domain. PKC $\beta$  phosphorylation is selective for p110 $\gamma$ -p84  
44 compared to p110 $\gamma$ -p101, driven by differential dynamics of the helical domain of these  
45 different complexes. Nanobody binding prevented PKC $\beta$  mediated phosphorylation.  
46 Overall, this work shows an unexpected allosteric regulatory role of the helical domain  
47 of p110 $\gamma$  that is distinct between p110 $\gamma$ -p84 and p110 $\gamma$ -p101, and reveals how this can be  
48 modulated by either phosphorylation or allosteric inhibitory binding partners. This opens  
49 possibilities of future allosteric inhibitor development for therapeutic intervention.

50

51

## 52 Introduction

53 The class I phosphoinositide 3 kinases (PI3Ks) are master regulators of myriad  
54 functions through their generation of the lipid signalling molecule phosphatidylinositol  
55 3,4,5-trisphosphate (PIP<sub>3</sub>) downstream of cell surface receptors (Burke and Williams,  
56 2015; Rathinaswamy and Burke, 2019; Vanhaesebroeck et al., 2021; Vasan and Cantley,  
57 2022). The class I PI3Ks can be further subdivided into the class IA and class IB  
58 subfamilies, with class IB PI3Ks being critical in immune signalling, and are composed  
59 of a single p110 $\gamma$  catalytic subunit that can bind to either a p101 or p84 regulatory subunit  
60 (Hawkins and Stephens, 2015; Lanahan et al., 2022; Okkenhaug, 2013). The two PI3K $\gamma$   
61 complexes (either p110 $\gamma$ -p84 or p110 $\gamma$ -p101) play essential and independent roles in both  
62 the adaptative and innate immune systems. PI3K $\gamma$  has shown promise as a therapeutic  
63 target, primarily as an immunomodulator of the tumor microenvironment leading to  
64 enhanced anti-tumor immune responses (De Henau et al., 2016; Kaneda et al., 2016b).  
65 Multiple isoform selective small molecule ATP competitive inhibitors of p110 $\gamma$  are in  
66 clinical trials for multiple forms of human cancers (Li et al., 2021). However, all inhibitors  
67 currently developed towards p110 $\gamma$  act as ATP competitive inhibitors, showing equal  
68 potency against both p110 $\gamma$ -p84 or p110 $\gamma$ -p101 complexes.

69 Detailed experiments on the role of p110 $\gamma$  in mice show that knockout of both p101  
70 and p84 leads to PIP<sub>3</sub> levels that are equivalent to knockout of p110 $\gamma$ , showing that all  
71 cellular PI3K $\gamma$  activity requires the presence of either a p84 or p101 regulatory subunit  
72 (Rynkiewicz et al., 2020). The two complexes are differentially activated by membrane  
73 localised receptors, including G-protein coupled receptors (Li et al., 2000; Stephens et  
74 al., 1997), Ras (Jin et al., 2020; Kurig et al., 2009), toll like receptors (TLRs) (Luo et al.,  
75 2018), and the IgE antigen receptor (Laffargue et al., 2002; Walser et al., 2013). This  
76 leads to the different complexes driving unique immune responses, with p110 $\gamma$ -  
77 p101 involved in chemotaxis in neutrophils (Bohnacker et al., 2009; Deladeriere et al.,  
78 2015), and p110 $\gamma$ -p84 involved in reactive oxide production. Differential activation of  
79 unique PI3K $\gamma$  complexes downstream of GPCRs and Ras is caused by the ability of p101  
80 to directly bind to G $\beta\gamma$  subunits downstream of activated GPCRs, with this being lost in

81 p84, making p110 $\gamma$ -p84 activation by G $\beta\gamma$  dependent on Ras mediated membrane  
82 recruitment (Rathinaswamy et al., 2023; Kurig et al., 2009; Rynkiewicz et al., 2020).  
83 Activation of PI3K $\gamma$  downstream of the IgE antigen receptor is driven by calcium mediated  
84 activation of protein kinase C $\beta$ , leading to the selective phosphorylation and activation of  
85 p110 $\gamma$  at S582 (Walser et al., 2013), with this putatively only occurring in p110 $\gamma$ -p84 and  
86 not p110 $\gamma$ -p101. The full molecular mechanisms underlying how phosphorylation of p110 $\gamma$   
87 is selective for different p84 or p101 complexes, and how it activates lipid kinase activity  
88 are poorly understood.

89         Extensive biophysical approaches including cryo electron microscopy (cryo-EM),  
90 X-ray crystallography, and hydrogen deuterium exchange mass spectrometry (HDX-MS)  
91 have provided extensive insight into the molecular underpinnings of how p110 $\gamma$   
92 associates with both p101 and p84, how they are differentially activated by Ras and  
93 GPCR signals, and how they can be activated on lipid membranes (Pacold et al., 2000;  
94 Walker et al., 1999; Rathinaswamy et al., 2021c, 2021a; Gangadhara et al., 2019; Vadas  
95 et al., 2013; Rathinaswamy et al., 2023). The p110 $\gamma$  catalytic subunit is composed of an  
96 adaptor binding domain (ABD), a Ras binding domain (RBD), a C2 domain, a helical  
97 domain, and a bi-lobal kinase domain (Rathinaswamy et al., 2021a; Walker et al., 1999).  
98 A set of helices positioned C-terminal to the activation loop in the kinase domain play a  
99 critical role in regulating activity, with this region referred to as the regulatory motif  
100 (Rathinaswamy et al., 2021c). The p110 $\gamma$  isoform is unique in that it is inhibited in the  
101 absence of a regulatory subunit, with this driven by an autoinhibitory conformation of the  
102 regulatory motif, that is proposed to require membrane association to disrupt  
103 (Gangadhara et al., 2019). The regulatory motif is a common site of activating mutations  
104 in the other class I PI3K isoforms (Jenkins et al., 2023), with p110 $\gamma$  having rare activating  
105 oncogenic mutants in this region (Rathinaswamy et al., 2021c). The p110 $\gamma$  subunit  
106 interacts with both p84 and p101 at an interface composed of the C2 domain, and the  
107 linkers between the RBD-C2 and C2-helical domains (Rathinaswamy et al., 2023, 2021a).  
108 The p110 $\gamma$ -p84 complex forms a more dynamic complex compared to p110 $\gamma$ -p101  
109 (Rathinaswamy et al., 2023; Shymanets et al., 2013), however, no clear unique regulatory  
110 role of this difference in dynamics has been identified.

111 The fundamental roles of p110 $\gamma$  in inflammatory processes has made it a  
112 therapeutic target in many pathological conditions, including asthma (Campa et al., 2018),  
113 arthritis (Camps et al., 2005), obesity (Becattini et al., 2011; Breasson et al., 2017), and  
114 cancer (De Henau et al., 2016; Kaneda et al., 2016a, 2016b). There are significant side  
115 effects from non-isoform selective PI3K inhibitors (Bohnacker et al., 2017;  
116 Vanhaesebroeck et al., 2021), which has driven the development of highly p110 $\gamma$  selective  
117 small molecule inhibitors (Bell et al., 2012; Evans et al., 2016; Gangadhara et al., 2019).  
118 However, all p110 $\gamma$  inhibitors will target both p110 $\gamma$ -p101 and p110 $\gamma$ -p84, so there is a  
119 potential for the development of allosteric inhibitors outside of the ATP binding site. Initial  
120 promise has been reported for the development of class IA p110 $\alpha$  oncogene specific  
121 allosteric inhibitors. However, further investigation of the molecular mechanisms  
122 underlying p110 $\gamma$  regulation will be required for the discovery of regions that can be  
123 targeted for allosteric inhibitor development.

124 Here we report critical roles of the helical domain of p110 $\gamma$  in both activation and  
125 inhibition of lipid kinase activity. We characterised an allosteric inhibitory nanobody (NB7)  
126 that potently inhibits p110 $\gamma$  activity. Cryo-EM was used to define the inhibitory interface,  
127 which is composed of the helical domain, the ABD-RBD linker, and the regulatory motif  
128 of the kinase domain of p110 $\gamma$ . The region that the nanobody binds to is in close spatial  
129 proximity to a previously identified PKC $\beta$  phosphorylation site (S582) in the helical  
130 domain, and oncogenic activating mutants in the regulatory motif. We fully characterised  
131 the activity and dynamics of stoichiometrically PKC $\beta$  phosphorylated p110 $\gamma$ , leading to  
132 the discovery of a novel additional phosphorylation site (S594/S595). PKC $\beta$   
133 phosphorylation was highly selective for p110 $\gamma$  and p110 $\gamma$ -p84, with limited  
134 phosphorylation of p110 $\gamma$ -p101. Hydrogen deuterium exchange mass spectrometry  
135 (HDX-MS) analysis showed that phosphorylation of p110 $\gamma$  leads to unfolding of the N-  
136 terminal region of the helical domain, and increased kinase activity. The presence of the  
137 inhibitory nanobody significantly blocks PKC $\beta$  phosphorylation, with phosphorylated  
138 p110 $\gamma$  showing no detectable binding to NB7. Overall, this work provides unique insight  
139 into the critical role of the helical domain in controlling p110 $\gamma$  activity, and how

140 phosphorylation and binding partners can modify this regulation. It also reveals a unique  
141 binding site located at the interface of the helical and kinase domain that can be targeted  
142 for future allosteric inhibitor design.

143

## 144 **Results**

### 145 *Molecular mechanism of nanobody inhibition of p110 $\gamma$*

146 We previously identified multiple nanobodies that inhibited the activity of p110 $\gamma$ .  
147 One from this group (denoted NB7 throughout the manuscript) potently inhibited the  
148 membrane mediated activation of p110 $\gamma$ -p84 by both Ras and G $\beta\gamma$ , with HDX-MS  
149 experiments mapping the NB7 binding interface to the RBD, helical and kinase domains  
150 (Rathinaswamy et al., 2021b). We originally hypothesized that NB7 worked by sterically  
151 inhibiting Ras binding to the RBD domain of p110 $\gamma$ . To further explore the molecular  
152 mechanism of inhibition we purified all complexes of p110 $\gamma$  (p110 $\gamma$  apo, p110 $\gamma$ -p84,  
153 p110 $\gamma$ -p101) along with the NB7 nanobody. The SDS-PAGE of all proteins utilised in this  
154 study are shown in the source data file included in the supplemental information.

155 To define the mechanism concerning how NB7 inhibits PI3K activity we analyzed  
156 how this nanobody inhibited all class IB PI3K complexes (p110 $\gamma$ , p110 $\gamma$ -p84, p110 $\gamma$ -p101)  
157 upon activation by lipidated G $\beta\gamma$  subunits. Intriguingly, we found that all three forms of  
158 p110 $\gamma$  were potently inhibited by NB7 (Fig. 1A). While the IC<sub>50</sub> measured for the three  
159 complexes was different, this is likely mainly due to the dramatic difference in protein  
160 required to measure lipid kinase activity *in vitro* (~300 nM for p110 $\gamma$  apo/p110 $\gamma$ -p84, and  
161 ~10 nM for p110 $\gamma$ -p101, respectively). This suggested that the mechanism of inhibition  
162 was not driven by a steric block of Ras association through the RBD, as previously  
163 proposed (Rathinaswamy et al., 2021b). We examined the binding of this nanobody to all  
164 complexes using bilayer interferometry (BLI). The nanobody bound equivalently tightly  
165 to all complexes, with ~2 nM potency for p110 $\gamma$ , p110 $\gamma$ -p84, and p110 $\gamma$ -p101 (Fig. 1B).  
166 We also tested binding of the nanobody to all class IA PI3Ks, and there was no detectable  
167 binding to p110 $\alpha$ , p110 $\beta$ , and p110 $\delta$  (Fig. 1C).

168 To further understand the mechanism by which this nanobody blocked lipid kinase  
169 activity we measured the bulk membrane recruitment dynamics of fluorescently labeled  
170 Dy647-p84-p110 $\gamma$  on supported lipid bilayers (SLBs) using Total Internal Reflection  
171 Fluorescence (TIRF) Microscopy. We found that the nanobody had no effect on  
172 membrane recruitment of p110 $\gamma$ -p84 on bilayers containing membrane-tethered  
173 Ras(GTP) and G $\beta\gamma$  (Fig. 1D-F). Membrane binding was not affected when the nanobody  
174 was spiked into samples containing membrane associated Dy647-p84-p110 $\gamma$  (Fig 1D).  
175 Similarly, pre-incubation of Dy647-p84-p110 $\gamma$  with 500 nM NB7 did not perturb membrane  
176 association of the kinase when flowed over a supported membrane (Fig. 1E).

177 We wanted to define the molecular mechanism of how nanobody NB7 was a potent  
178 allosteric inhibitor of lipid kinase activity. We purified the complex of nanobody NB7 bound  
179 to p110 $\gamma$ -p84 to homogeneity by gel filtration. Using this sample, we obtained a cryo-EM  
180 reconstruction of the complex of nanobody (NB7)-bound p110 $\gamma$  at 3.0-Å overall resolution  
181 from 149,603 particles (Figs. 2A-D, S1 and supplemental table 1). The density map was  
182 of sufficient quality to perform automated and manual construction of the p110 $\gamma$ -NB7  
183 complex, with unambiguous building of the interfacial contacts between NB7 and p110 $\gamma$ .  
184 Nanobody binding did not induce any large-scale conformational changes of p110 $\gamma$ , as  
185 the structure of p110 $\gamma$  bound to NB7 was similar to the apo p110 $\gamma$  crystal structure or  
186 p110 $\gamma$ -p101 cryo-EM structure (Fig. S2). The lowest local resolution was in the ABD  
187 domain, with increased B-factors of the ABD in the p110 $\gamma$ -NB7 structure compared to  
188 p110 $\gamma$ -p101 (Fig. S2). This is consistent with the concept that ABD flexibility plays an  
189 important role in class I PI3K regulation (Liu et al., 2022).

190 The interface between NB7 and p110 $\gamma$  was extensive, with ~1200 Å<sup>2</sup> of buried  
191 surface area, with interactions of the ABD-RBD linker, N-terminus of the helical domain,  
192 and the regulatory motif at the turn between  $\kappa\alpha 8$ - $\kappa\alpha 9$  (1022-1026aa). This location in the  
193 regulatory motif is where both activating oncogenic (R1021C) and inhibitory loss of  
194 function mutants have been identified (R1021P) (Takeda et al., 2019), as well as a  
195 putative inhibitory phosphorylation site (T1024) (Perino et al., 2011). The resolution was  
196 sufficient to unambiguously build the three complementarity determining region (CDR)

197 loops of NB7 that mediate target selectivity (Fig. 2E-F). The interface is primarily  
198 hydrophobic, with only 8 hydrogen bonds, and 1 electrostatic interaction among the 33  
199 interfacial residues of NB7. A pocket formed between the helical domain and the ABD-  
200 RBD linker forms the majority of the interface, with extensive interactions with the long  
201 CDR3. The CDR1 loop packed up against the N-terminal section of the helical domain,  
202 with the CDR2 loop forming the interface with the regulatory motif. Previous study of  
203 oncogenic mutants in the regulatory motif of p110 $\gamma$  showed that increased dynamics  
204 mediated by these mutants increased kinase activity, putatively by breaking the  
205 autoinhibitory tryptophan lock in  $\kappa\alpha 12$  of the regulatory motif. Therefore, rigidifying the  
206 regulatory motif likely explains the molecular basis for how it prevents kinase activity. The  
207 nanobody interface is distinct from the predicted G $\beta\gamma$  interface (Rathinaswamy et al.,  
208 2023) and the experimentally resolved Ras interface (Pacold et al., 2000), explaining why  
209 it can still be membrane recruited by these stimuli.

210

### 211 *p110 $\gamma$ activation by helical domain phosphorylation*

212 To further understand the potential role helical domain dynamics in regulating  
213 p110 $\gamma$  activity we searched for any possible regulatory roles of this in PI3K signalling. It  
214 has been previously identified that p110 $\gamma$  is directly phosphorylated by the protein kinase  
215 PKC $\beta$  on residue S582 in the helical domain (Walser et al., 2013). S582 is located on the  
216 interior of the helical domain, and would not be expected to be exposed when the N-  
217 terminal region of the helical domain is folded (Fig. 3A). To understand this better at a  
218 molecular level, we purified a catalytic fragment of PKC $\beta$  and performed protein  
219 phosphorylation reactions on p110 $\gamma$  apo, p110 $\gamma$ -p84, and p110 $\gamma$ -p101. We identified a  
220 phosphorylated peptide containing S582, and surprisingly, we found an additional p110 $\gamma$   
221 phosphorylation site at S594/S595 (Fig. 3B, Fig. S3). The S594/S595 site is also located  
222 in the N-terminal region of the helical domain, and is even more buried than S582, and  
223 would not be expected to be exposed when this region is folded (Fig. 3A). Dose response  
224 curves of PKC $\beta$  treatment were carried out for p110 $\gamma$  (Fig. 3C), p110 $\gamma$ -p84 (Fig. 3D), and  
225 p110 $\gamma$ -p101 (Fig. 3E). Both p110 $\gamma$  and p110 $\gamma$ -p84 showed similar dose response curves

226 for PKC $\beta$  treatment, with similar curves for S582 and S594/S595. The p110 $\gamma$ -p101  
227 complex was only very weakly phosphorylated, with <100-fold lower levels compared to  
228 p110 $\gamma$  and p110 $\gamma$ -p84 (Fig. 3E). This is consistent with the helical domain in p110 $\gamma$  being  
229 more rigid when bound to p101, compared to either bound to p84 or p110 $\gamma$  alone.

230 To provide additional insight into the molecular mechanisms underlying p110 $\gamma$   
231 phosphorylation we carried out hydrogen deuterium exchange mass spectrometry (HDX-  
232 MS) experiments on p110 $\gamma$  and phosphorylated p110 $\gamma$  (90.8% phosphorylated S594/595,  
233 92% phosphorylated S582) (Fig. 4A). The full data underlying the experiment is available  
234 in the source data, and data processing information is in supplemental table 2. We have  
235 previously observed that the N-terminal region of the helical domain of apo p110 $\gamma$   
236 (residues spanning 557-630aa) shows isotope profiles that are consistent with EX1 H/D  
237 exchange kinetics (Rathinaswamy et al., 2021b, 2021c; Vadas et al., 2013; Walser et al.,  
238 2013). This is indicative of cooperative unfolding of extended protein regions, with H/D  
239 exchange occurring faster than the refolding event. This region is where the PKC  
240 phosphorylation sites are located, and may explain how the buried residues S582 and  
241 S594/S595 can be exposed to PKC. This is compatible with the observation that p110 $\gamma$ -  
242 p101 is protected from phosphorylation, as it does not show EX1 kinetics in this region,  
243 whereas both p110 $\gamma$  and p110 $\gamma$ -p84 do (Rathinaswamy et al., 2021a).

244 When we compared phosphorylated p110 $\gamma$  (>90.8% as measured by mass  
245 spectrometry at both sites) to unphosphorylated p110 $\gamma$  we observed extensive increases  
246 in dynamics in the C2, helical domain and kinase domain (Fig. 4A-D). The largest  
247 increases in exchange upon phosphorylation were located in the N-terminal region of the  
248 helical domain, with the peptides directly adjacent to the phosphorylation site showing  
249 almost complete deuterium incorporation at the earliest time points of exchange. This is  
250 indicative of significant disruption of the alpha helical secondary structure in this region.  
251 When we examined the exchange profiles in this region they still underwent EX1 kinetics  
252 (Fig. 4C), however, phosphorylated p110 $\gamma$  was enriched in the more fully deuterated  
253 species. In addition to the regions in the helical domain, a portion of the regulatory motif  
254 of the kinase domain also showed increased deuterium exposure. This included the  $\kappa\alpha$ 9-

255  $\kappa\alpha 12$  helices that surround the activation loop of p110 $\gamma$ . These increases in exchange  
256 were similar to those we had observed in a R1021C oncogenic activating mutant of  
257 *PIK3CG* (Rathinaswamy et al., 2021c).

258 To further explore the potential role of phosphorylation in mediating p110 $\gamma$  activity,  
259 we examined the kinase activity of p110 $\gamma$  for both basal ATPase and lipid membranes.  
260 Assays measured the hydrolysis of ATP to ADP, with this acting as a surrogate for PIP<sub>3</sub>  
261 production in the membrane assay. PKC $\beta$ -mediated phosphorylation enhanced the  
262 ATPase activity of p110 $\gamma$  ~2-fold in both the absence and presence of membranes (Fig.  
263 4E).

264

### 265 *Nanobody blocks p110 $\gamma$ phosphorylation*

266 As NB7 bound at the interface of the helical and kinase domains that is exposed  
267 upon PKC phosphorylation of p110 $\gamma$  we hypothesized that the nanobody would likely alter  
268 phosphorylation. We carried out PKC phosphorylation of p110 $\gamma$ , p110 $\gamma$ -p101 and p110 $\gamma$   
269 bound to NB7. The presence of NB7 showed even lower phosphorylation than p110 $\gamma$ -  
270 p101, with almost complete abrogation of phosphorylation at both sites (Fig. 5A-B). We  
271 also wanted to determine whether p110 $\gamma$  phosphorylation reciprocally perturbed NB7  
272 binding. BLI experiments showed that there was no detectable binding of NB7 to  
273 phosphorylated p110 $\gamma$  (Fig. 5C-D), consistent with phosphorylation disrupting the N-  
274 terminal region of the p110 $\gamma$  helical domain. In addition, lipid kinase assays using  
275 phosphorylated p110 $\gamma$  showed no detectable difference in activity when measured in the  
276 absence and presence nanobody (Fig. 5E).

277

## 278 **Discussion**

279 Here we find that the helical domain is a central regulator of the p110 $\gamma$  catalytic  
280 subunit of class IB PI3K, with modulation of helical dynamics through binding partners or  
281 PTMs able to either increase or decrease lipid kinase activity. These results expand on  
282 previous work defining the helical domain as a central regulator of class IA PI3Ks, where  
283 the nSH2 domain of the p85 regulatory subunits makes inhibitory interactions that

284 significantly inhibit lipid kinase activity of all class IA catalytic subunits (p110 $\alpha$ , p110 $\beta$ ,  
285 and p110 $\delta$ ) (Mandelker et al., 2009; Miled et al., 2007; Burke and Williams, 2013; Burke,  
286 2018). This inhibitory interaction in class IA PI3Ks is disrupted in human cancers (helical  
287 hotspot mutations in *PIK3CA*) (Samuels et al., 2004) and immune disorders (helical  
288 mutations in *PIK3CD* in APDS1) (Angulo et al., 2013; Lucas et al., 2014). Class IB PI3Ks  
289 are unique compared to class IA PI3Ks, as they are not inhibited by p101 and p84  
290 regulatory subunits, but instead potentiate GPCR activation. This lack of inhibition is due  
291 to the distinct binding interface of class IB PI3K regulatory subunits compared to class IA  
292 regulatory subunits, with only class IA regulatory subunits making direct inhibitory  
293 interactions with the kinase and helical domains of p110 catalytic subunits  
294 (Rathinaswamy et al., 2021a). Here we show that a unique surface at the interface of the  
295 helical and kinase domains of p110 $\gamma$  is a potential site for the development of novel  
296 allosteric inhibitors that modulate p110 $\gamma$  activity.

297         The previously identified inhibitory nanobody (NB7) (Rathinaswamy et al., 2021b)  
298 bound with high affinity and inhibited all complexes of p110 $\gamma$ . The nanobody interface is  
299 distinct from how the nSH2 inhibits class IA PI3K activity, as its binding site is on the  
300 opposite face of the helical domain (Fig. 6A). The mechanism of inhibition is also distinct,  
301 as the nSH2-helical interaction plays a critical role in preventing membrane recruitment  
302 of inhibited class I PI3Ks, with removal of this interface either through pYXXM motif  
303 binding, or oncogenic mutations leading to increased membrane recruitment (Burke et  
304 al., 2012, 2011; Zhang et al., 2011). Analysis of the nanobody binding site compared to  
305 the structure of HRas-p110 $\gamma$  or the HDX-MS supported AlphaFold-multimer prediction of  
306 G $\beta\gamma$ -p110 $\gamma$  (Rathinaswamy et al., 2023) shows that nanobody binding does not sterically  
307 block complex formation (Fig. 6B). This is consistent with it not blocking membrane  
308 recruitment by Ras/G $\beta\gamma$ . The nanobody inhibited ATP turnover both in solution and on  
309 membranes, suggesting that it prevents formation of a catalytically competent  
310 conformation of p110 $\gamma$ , but still allows for membrane recruitment. Further development of  
311 small molecule allosteric binding partners in this allosteric pocket between the kinase and  
312 helical domain may reveal the specific molecular interactions in this pocket that mediate  
313 inhibition.

314 Oncogenic mutations are frequent in the class IA PI3K $\alpha$  encoded by *PIK3CA*, with  
315 this being the 2<sup>nd</sup> most frequently mutated gene in human cancer (Lawrence et al., 2014).  
316 Mutations in p110 $\gamma$  encoded by *PIK3CG* in cancer are less frequent, however, they can  
317 still provide insight into regulatory mechanisms that control activity. Oncogenic mutations  
318 in the kinase domain (R1021C) and helical domain (E581K) are in close proximity to the  
319 nanobody binding site, and both would be expected to disrupt the stability of the helical  
320 domain or regulatory motif of the kinase domain (Fig. 6C). In addition to these mutations  
321 there are also multiple post-translational modifications that occur in this region, including  
322 inhibitory phosphorylation at T1024 (Perino et al., 2011), and activating phosphorylation  
323 at S582 (Walser et al., 2013). PKC $\beta$  is activated downstream of the IgE receptor in mast  
324 cells (Walser et al., 2013), but the full details of how this activates PI3K has been unclear.  
325 We identified an additional PKC $\beta$  phosphorylation site located in the helical domain  
326 (S594/S595) (Fig. 6C). Both the S582 and S594/S595 sites are not surface accessible  
327 and would require a transient opening of the helical domain for kinase accessibility. HDX-  
328 MS analysis of the helical domain of p110 $\gamma$  has shown that it is more dynamic than other  
329 class I PI3K isoforms (Burke and Williams, 2013; Walser et al., 2013), with the presence  
330 of the p101 regulatory subunit dramatically decreasing helical domain dynamics (Vadas  
331 et al., 2013). This putative mechanism of helical domain dynamics driving PKC $\beta$   
332 phosphorylation is consistent with our observation that p101 subunits decreased p110 $\gamma$   
333 phosphorylation >100-fold. PKC $\beta$  phosphorylation of p110 $\gamma$  leads to increased dynamics  
334 in both the helical and kinase domains with increased kinase activity, although only  
335 weakly compared to full activation by either membrane localised Ras or G $\beta\gamma$ . This  
336 increase was observed with both membrane and soluble substrate, so likely is not driven  
337 by altered membrane recruitment.

338 Overall, our biophysical and biochemical analysis of modulators of helical domain  
339 dynamics reveal the critical role of this domain in regulating class IB PI3K activity. This  
340 raises possibilities for development of small molecule modulators that may either increase  
341 or decrease helical domain dynamics, leading to either activation or inhibition. The high-  
342 resolution structure of an allosteric inhibitor nanobody provide initial insight into which  
343 pockets can specifically be targeted. Multiple ATP competitive p110 $\gamma$  selective inhibitors

344 are in clinical trials for human cancers (Li et al., 2021), with many having significant side  
345 effects. The identification of novel inhibitory strategies provides new opportunities for  
346 targeting p110 $\gamma$  dysregulation in human disease.

347

## 348 **Acknowledgements**

349 J.E.B. is supported by the Canadian Institute of Health Research (CIHR, 168998),  
350 and the Michael Smith Foundation for Health Research (MSFHR, scholar 17686). C.K.Y.  
351 is supported by CIHR (FDN-143228, PJT-168907) and the Natural Sciences and  
352 Engineering Research Council of Canada (RGPIN-2018-03951). S.D.H. is supported by  
353 an NSF CAREER Award (MCB-2048060). This research project was supported in part by  
354 the UBC High Resolution Macromolecular Cryo-Electron Microscopy Facility (HRMEM).  
355 A portion of this research was supported by NIH grant U24GM129547 and performed at  
356 the PNCC at OHSU and accessed through EMSL (grid.436923.9), a DOE Office of  
357 Science User Facility sponsored by the Office of Biological and Environmental Research.  
358 We appreciate help from Theo Humphreys and Rose Marie Haynes with data collection  
359 at PNCC. Competing Interests: The authors declare that they have no competing  
360 interests.

361

## 362 **Conflict of Interest statement**

363 JEB reports personal fees from Scorpion Therapeutics, Reactive therapeutics and  
364 Olema Oncology; and research grants from Novartis. Other authors declare no competing  
365 interests.

366

## 367 **Methods**

<b>Resources table</b>	SOURCE	IDENTIFIER
<b>Bacterial and virus strains</b>		
E.coli XL10-GOLD KanR Ultracompetent Cells	Agilent	200317
E.coli DH10EMBacY Competent Cells	Geneva Biotech	DH10EMBacY
<b>Chemicals, peptides, and recombinant proteins</b>		
Deuterium Oxide 99.9%	Sigma	151882
Guanosine 5'-diphosphate (GDP) sodium salt hydrate	Sigma	G7127-100MG
Guanosine 5'-triphosphate (GTP) sodium salt hydrate	Sigma	G8877-250MG
Sodium deoxycholate	Sigma	D6750

Polyoxyethylene (10) lauryl ether	Sigma	P9769
CHAPS, Molecular Biology Grade	EMD Millipore	220201
Phosphatidylserine (Porcine Brain)	Avanti	840032C
Phosphatidylethanolamine (Egg yolk)	Sigma	P6386
Cholesterol	Sigma	47127-U
Phosphatidylcholine (Egg yolk)	Avanti	840051C
Phosphatidylinositol-4,5-bisphosphate (Porcine Brain)	Avanti	840046
Sphingomyelin (Egg yolk)	Sigma	S0756
1,2-dioleoyl-sn-glycero-3-phosphocholine (DOPC)	Avanti	850375C
1,2-dioleoyl-sn-glycero-3-phospho-L-serine (18:1, DOPS)	Avanti	840035C
1,2-dioleoyl-sn-glycero-3-phosphoethanolamine-N-[4-(p-maleimidomethyl)cyclohexane-carboxamide] (18:1 MCC-PE)	Avanti	780201C
10 mg/mL beta casein solution	ThermoFisher	37528
10x PBS [pH 7.4]	Corning	46-013-CM
glucose oxidase from <i>Aspergillus niger</i> (225 U/mg)	Biophoretics	B01357.02
catalase	Sigma	C40-100MG Bovine Liver
Trolox	Cayman Chemicals	10011659
Dyomics 647 maleimide dye	Dyomics	647P1-03
Coenzyme A	Sigma	C3019
Sulfuric acid	Sigma	58105-2.5L-PC
C-Flat 2/2-T grids	FisherScientific	50-192-8327
<b>Critical commercial assays</b>		
Transcreener ADP2 FI Assay (1,000 Assay, 384 Well)	BellBrook Labs	3013-1K
<b>Deposited data</b>		
PDB coordinate file for p110 $\gamma$ -NB7 structure	PDB	8DP0
EM density file for p110 $\gamma$ -NB7 complex	EMD	EMD-27627
HDX-MS and phosphorylation proteomics data	PRIDE	PXD040765
<b>Oligonucleotides</b>		
Fwd primer for amplifying KD of PKC $\beta$ II GTATTTTCAGGGCgcccgtaccACGACCAACTGTCT CCAAATTTG	Sigma	MR51F
Rvs primer for amplifying KD of PKC $\beta$ II gactcgagcggccgcTTATAGCTCTTGACTTCGGGTTTTA AAAATTCAG	Sigma	MR51R
Fwd primer for amplifying N term of PKC $\beta$ II CCATCACggatctggcggtagtATGGCTGACCCGGCTGCG	Sigma	MR52F
Rvs primer for amplifying N term of PKC $\beta$ II GCCCTGAAAATACAGGTTTTCTTTCTTCCGGGAC CTTGTTCCC	Sigma	MR52R
Fwd primer for adding stop codon to PKC $\beta$ II AGTCAAGAGCTAAgcccgcctcgagtctagagcctgc	Sigma	MR56F
Rvs primer for adding stop codon to PKC $\beta$ II gactcgagcggccgcTTAGCTCTTGACTTCGGGTTTTAAA AATTCAG	Sigma	MR56R
<b>Recombinant DNA</b>		
pMultiBac-G $\beta$ 1/G $\gamma$ 2	PMID:34452907	pOP737

pACEBac1-hsp110 $\gamma$	PMID:34452907	MR30
pMultiBac-hsp110 $\gamma$ -ssp101	PMID:34452907	MR22
pMultiBac-hsp110 $\gamma$ -mmp84	PMID:34452907	MR24
pFastBac HRas G12V	PMID:34452907	BS9
biGBac hsp110 $\gamma$ /ybbr-hsp84	PMID:36842083	HP28
biGBac hsp110 $\gamma$ /ybbr-hsp101	PMID:36842083	HP29
his6-GST-PrescissionProtease-SNAP-RBD(K65E)	PMID:34452907	pSH936
his6TEV-HRas(1-184aa) C118S, C181S	PMID:34452907	pSH414
his6-G $\gamma$ 2, SNAP-G $\beta$ 1 (DUAL FastBac)	PMID:34452907	pSH651
pACEBAC-PKC $\beta$ II (internal tev cleavage site)	This paper	pMR56
pFASTBac p110 $\alpha$	PMID: 28515318	pOV1181
pFASTBac p110 $\beta$	PMID: 28515318	pOV1182
pFASTBac p110 $\delta$	PMID: 28515318	pOV1183
pFASTBac p85 $\beta$	This paper	EX21
<b>Software and algorithms</b>		
COOT-0.9.4.1	CCP4	<a href="https://www2.mrc-lmb.cam.ac.uk/personal/pemsley/cool/">https://www2.mrc-lmb.cam.ac.uk/personal/pemsley/cool/</a>
Phenix-1.19.1	Open source	<a href="https://www.phenix-online.org/">https://www.phenix-online.org/</a>
PDBePISA (Proteins, Interfaces, Structures and Assemblies)	EMBL-EBI	<a href="https://www.ebi.ac.uk/pdbe/pisa/pistart.html">https://www.ebi.ac.uk/pdbe/pisa/pistart.html</a>
ESPrpt 3.0	Robert et al NAR 2014	<a href="https://esprpt.ibcp.fr">https://esprpt.ibcp.fr</a>
HDEaminer	Sierra Analytics	<a href="http://massspec.com/hdeaminer">http://massspec.com/hdeaminer</a>
GraphPad Prism 7	GraphPad	<a href="https://www.graphpad.com">https://www.graphpad.com</a>
PyMOL	Schroedinger	<a href="http://pymol.org">http://pymol.org</a>
Compass Data Analysis	Bruker	<a href="https://www.bruker.com">https://www.bruker.com</a>
ChimeraX	UCSF	<a href="https://www.rbvi.ucsf.edu/chimera/">https://www.rbvi.ucsf.edu/chimera/</a>
ImageJ/Fiji	ImageJ	<a href="https://imagej.net/software/fiji/">https://imagej.net/software/fiji/</a>
Nikon NIS elements	Nikon	<a href="https://www.microscope.healthcare.nikon.com/products/software/nis-elements">https://www.microscope.healthcare.nikon.com/products/software/nis-elements</a>
cryoSPARC v.3.3.2	Structura Biotechnology	<a href="https://cryosparc.com/">https://cryosparc.com/</a>
<b>Other</b>		
Sf9 insect cells for expression	Expression Systems	94-001S
Insect cell media	Expression Systems	96-001-01
Hellmanex III cleaning solution	Fisher	14-385-864
6-well sticky-side chamber	IBIDI	80608

369

### 370 *Plasmid Generation*

371 Plasmids encoding Homo sapiens p110 $\gamma$  (human), Mus musculus p84 (mouse), Sus  
372 scrofa p101 (porcine), and G $\beta\gamma$  were used as previously described (Rathinaswamy et al.,  
373 2023, 2021a). The class IA plasmids were also used as previously described (Dornan et  
374 al., 2017; Siempelkamp et al., 2017). The pDONR223-PRKCB2 (PKC $\beta$ II, uniprot  
375 identifier: P05771-2) was a gift from William Hahn & David Root (Addgene plasmid  
376 #23746; <http://n2t.net/addgene:23746>; RRID:Addgene\_23746) (Johannessen et al.,  
377 2010). The PKC $\beta$ II construct contains an internal TEV site that cleaves the catalytic  
378 domains from the C1/C2 regulatory domains (TEV site inserted between residues 320  
379 and 321 of PRKCB, uniprot identifier: P05771-2) and it was subcloned into a pACEBAC  
380 Sf9 expression vector for protein purification. For purification, a 10 $\times$  histidine tag, a 2 $\times$   
381 strep tag, and a tobacco etch virus protease cleavage site were cloned to the N terminus  
382 of the regulatory subunits for the complex and to p110 $\gamma$  and PKC $\beta$ II for constructs without  
383 regulatory subunits. Full details of the plasmids are included in the resource table.

384

### 385 *Virus Generation and Amplification:*

386 The plasmids encoding genes for insect cell expression were transformed into  
387 DH10MultiBac cells (MultiBac, Geneva Biotech) to generate baculovirus plasmid  
388 (bacmid) containing the genes of interest. Successful generation was identified by blue-  
389 white colony screening and the bacmid was purified using a standard isopropanol-ethanol  
390 extraction method. Bacteria were grown overnight (16 hours) in 3-5 mL 2xYT (BioBasic  
391 #SD7019). Cells were spun down and the pellet was resuspended in 300  $\mu$ L of 50 mM  
392 Tris-HCl, pH 8.0, 10 mM EDTA, 100 mg/mL RNase A. The pellet was lysed by the addition  
393 of 300  $\mu$ L of 1% sodium dodecyl sulfate (SDS) (W/V), 200 mM NaOH, and the reaction  
394 was neutralized by addition of 400  $\mu$ L of 3.0 M potassium acetate, pH 5.5. Following  
395 centrifugation at 21130 RCF and 4  $^{\circ}$ C (Rotor #5424 R), the supernatant was mixed with  
396 800  $\mu$ L isopropanol to precipitate bacmid DNA. Following centrifugation, the pelleted  
397 bacmid DNA was washed with 500  $\mu$ L 70% Ethanol three times. The pellet was then air  
398 dried for 1 minute and re-suspended in 50  $\mu$ L Buffer EB (10 mM Tris-Cl, pH 8.5; All buffers

399 from QIAprep Spin Miniprep Kit, Qiagen #27104). Purified bacmid was then transfected  
400 into Sf9 cells. 2 mL of Sf9 cells at  $0.6 \times 10^6$  cells/mL were aliquoted into a 6-well plate and  
401 allowed to attach to form a confluent layer. Transfection reactions were prepared mixing  
402 8-12  $\mu$ g of bacmid DNA in 100  $\mu$ L 1xPBS and 12  $\mu$ g polyethyleneimine  
403 (Polyethyleneimine “Max” MW 40.000, Polysciences #24765, USA) in 100  $\mu$ L 1xPBS and  
404 the reaction was allowed to proceed for 20-30 minutes before addition to an Sf9  
405 monolayer containing well. Transfections were allowed to proceed for 5-6 days before  
406 harvesting virus containing supernatant as a P1 viral stock.

407 Viral stocks were further amplified by adding P1 to Sf9 cells at  $\sim 2 \times 10^6$  cells/mL  
408 (2/100 volume ratio). This amplification was allowed to proceed for 4-5 days and resulted  
409 in a P2 stage viral stock that was used in final protein expression. Harvesting of P2 viral  
410 stocks was carried out by centrifuging cell suspensions in 50 mL Falcon tubes at 2281  
411 RCF (Beckman GS-15). To the supernatant containing virus, 5-10% inactivated fetal  
412 bovine serum (FBS; VWR Canada #97068-085) was added and the stock was stored at  
413 4°C.

414

#### 415 *Expression and purification of PI3K $\gamma$ , PI3K $\alpha/\beta/\delta$ and PKC $\beta$ constructs:*

416 PI3K $\gamma$  and PKC $\beta$  constructs were expressed in Sf9 insect cells using the baculovirus  
417 expression system. Following 55 hours of expression, cells were harvested by  
418 centrifuging at 1680 RCF (Eppendorf Centrifuge 5810 R) and the pellets were snap-  
419 frozen in liquid nitrogen. The complex was purified through a combination of nickel affinity,  
420 streptavidin affinity and size exclusion chromatographic techniques.

421 Frozen insect cell pellets were resuspended in lysis buffer (20 mM Tris pH 8.0, 100  
422 mM NaCl, 10 mM imidazole pH 8.0, 5% glycerol (v/v), 2 mM  $\beta$ ME), protease inhibitor  
423 (Protease Inhibitor Cocktail Set III, Sigma)) and sonicated for 2 minutes (15s on, 15s off,  
424 level 4.0, Misonix sonicator 3000). Triton-X was added to the lysate to a final  
425 concentration of 0.1% and clarified by spinning at 15,000 RCF at 4°C for 45 minutes  
426 (Beckman Coulter JA-20 rotor). The supernatant was loaded onto a 5 mL HisTrap™ FF  
427 crude column (GE Healthcare) equilibrated in NiNTA A buffer (20 mM Tris pH 8.0, 100  
428 mM NaCl, 20 mM imidazole pH 8.0, 5% (v/v) glycerol, 2 mM  $\beta$ ME). The column was

429 washed with high salt NiNTA A buffer (20 mM Tris pH 8.0, 1 M NaCl, 20 mM imidazole  
430 pH 8.0, 5% (v/v) glycerol, 2 mM  $\beta$ ME), NiNTA A buffer, 6% NiNTA B buffer (20 mM Tris  
431 pH 8.0, 100 mM NaCl, 250 mM imidazole pH 8.0, 5% (v/v) glycerol, 2 mM  $\beta$ ME) and the  
432 protein was eluted with 100% NiNTA B. The eluent was loaded onto a 5 mL StrepTrap™  
433 HP column (GE Healthcare) equilibrated in gel filtration buffer (20mM Tris pH 8.5, 100  
434 mM NaCl, 50 mM Ammonium Sulfate and 0.5 mM TCEP). To purify *PI3K $\alpha/\beta/\delta$* , the  
435 purification protocol was performed as described above but instead the protein was eluted  
436 in PI3K $\alpha$  gel filtration buffer (20mM HEPES 7.5, 150mM NaCl, 0.5mM TCEP). The column  
437 was washed with the corresponding gel filtration buffer and loaded with tobacco etch virus  
438 protease. After cleavage on the column overnight, the PI3K $\gamma$  protein constructs were  
439 eluted in gel filtration buffer. The protein was concentrated in a 50,000 MWCO Amicon  
440 Concentrator (Millipore) to <1 mL and injected onto a Superdex™ 200 10/300 GL  
441 Increase size-exclusion column (GE Healthcare) equilibrated in gel filtration buffer. After  
442 size exclusion, the protein was concentrated, aliquoted, frozen, and stored at -80°C. For  
443 PKC $\beta$ , the protein was eluted from the strep column in gel filtration buffer, and the eluate  
444 was then loaded on a 1ml HisTrap™ FF column to remove the his tagged LipTev. The  
445 flowthrough was collected, and the column was washed with 2ml of gel filtration buffer.  
446 These fractions were pooled and concentrated and stored at -80°C.

447 To purify phosphorylated p110 $\gamma$ , the purification protocol as described above was  
448 performed but PKC $\beta$  was added to the strep column at a molar ratio of 1:3 (PKC $\beta$ II:p110)  
449 along with LipTEV, 20 mM MgCl<sub>2</sub> and 1mM ATP and allowed to incubate on ice for 4  
450 hours. The protein was eluted by adding 7 ml of gel filtration buffer and treated with a  
451 second dose of PKC $\beta$  (same ratio as above) and allowed to incubate on ice for another  
452 3 hours. For non-phosphorylated p110, same protocol was followed with the exception in  
453 the addition of PKC $\beta$ . Both the proteins were concentrated in a 50,000 MWCO Amicon  
454 Concentrator (Millipore) to <1 mL and injected onto a Superdex™ 200 10/300 GL  
455 Increase size-exclusion column (GE Healthcare) equilibrated in gel filtration buffer. The  
456 final phosphorylation level of the two sites was characterised by mass spectrometry, with  
457 these values being 92% and 90.8%, for S582 and S594/S595 respectively. After size  
458 exclusion, the protein was concentrated, aliquoted, frozen, and stored at -80°C.

459

460 *Expression and Purification of lipidated Gβγ for kinase activity assays:*

461 Full length, lipidated human *Gβγ* ( $G\beta_{1\gamma 2}$ ) was expressed in Sf9 insect cells and  
462 purified as described previously. After 65 hours of expression, cells were harvested, and  
463 the pellets were frozen as described above. Pellets were resuspended in lysis buffer (20  
464 mM HEPES pH 7.7, 100 mM NaCl, 10 mM βME, protease inhibitor (Protease Inhibitor  
465 Cocktail Set III, Sigma)) and sonicated for 2 minutes (15s on, 15s off, level 4.0, Misonix  
466 sonicator 3000). The lysate was spun at 500 RCF (Eppendorf Centrifuge 5810 R) to  
467 remove intact cells and the supernatant was centrifuged again at 25,000 RCF for 1 hour  
468 (Beckman Coulter JA-20 rotor). The pellet was resuspended in lysis buffer and sodium  
469 cholate was added to a final concentration of 1% and stirred at 4°C for 1 hour. The  
470 membrane extract was clarified by spinning at 10,000 RCF for 30 minutes (Beckman  
471 Coulter JA-20 rotor). The supernatant was diluted 3 times with NiNTA A buffer (20 mM  
472 HEPES pH 7.7, 100 mM NaCl, 10 mM Imidazole, 0.1% C12E10, 10mM βME) and loaded  
473 onto a 5 mL HisTrap™ FF crude column (GE Healthcare) equilibrated in the same buffer.  
474 The column was washed with NiNTA A, 6% NiNTA B buffer (20 mM HEPES pH 7.7, 25  
475 mM NaCl, 250 mM imidazole pH 8.0, 0.1% C12E10, 10 mM βME) and the protein was  
476 eluted with 100% NiNTA B. The eluent was loaded onto HiTrap™ Q HP anion exchange  
477 column equilibrated in Hep A buffer (20 mM Tris pH 8.0, 8 mM CHAPS, 2 mM  
478 Dithiothreitol (DTT)). A gradient was started with Hep B buffer (20 mM Tris pH 8.0, 500  
479 mM NaCl, 8 mM CHAPS, 2 mM DTT) and the protein was eluted in ~50% Hep B buffer.  
480 The eluent was concentrated in a 30,000 MWCO Amicon Concentrator (Millipore) to < 1  
481 mL and injected onto a Superdex™ 75 10/300 GL size exclusion column (GE Healthcare)  
482 equilibrated in Gel Filtration buffer (20 mM HEPES pH 7.7, 100 mM NaCl, 10 mM CHAPS,  
483 2 mM TCEP). Fractions containing protein were pooled, concentrated, aliquoted, frozen  
484 and stored at -80 °C.

485

486 *Expression and purification of nanobody:*

487 Nanobody NB7-PIK3CG with a C-terminal 6X His tag was expressed from a  
488 pMESy4 vector in the periplasm of WK6 *E.coli*. A 1L culture was grown to OD600 of 0.7

489 in Terrific Broth containing 0.1% glucose and 2mM MgCl<sub>2</sub> in the presence of 100 µg/mL  
490 ampicillin and was induced with 0.5 mM isopropyl-β-D-thiogalactoside (IPTG). Cells were  
491 harvested the following day by centrifuging at 2500 RCF (Eppendorf Centrifuge 5810 R)  
492 and the pellet was snap-frozen in liquid nitrogen. The frozen pellet was resuspended in  
493 15 mL of TES buffer containing 200 mM Tris pH 8.0, 0.5mM ethylenediaminetetraacetic  
494 acid (EDTA) and 500 mM Sucrose and was mixed for 45 minutes at 4°C. To this mixture,  
495 30 mL of TES buffer diluted four times in water was added and mixed for 45 minutes at  
496 4°C to induce osmotic shock. The lysate was clarified by centrifuging at 14,000 rpm for  
497 15 minutes (Beckman Coulter JA-20 rotor). Imidazole was added to the supernatant to  
498 final concentration of 10mM loaded onto a 5 mL HisTrap™ FF crude column (GE  
499 Healthcare) equilibrated in NiNTA A buffer (20 mM Tris pH 8.0, 100 mM NaCl, 20 mM  
500 imidazole pH 8.0, 5% (v/v) glycerol, 2 mM β-mercaptoethanol (βME)). The column was  
501 washed with high salt NiNTA A buffer (20 mM Tris pH 8.0, 1 M NaCl, 20 mM imidazole  
502 pH 8.0, 5% (v/v) glycerol, 2 mM βME), followed by 100% NiNTA A buffer, then a 6%  
503 NiNTA B wash buffer (20 mM Tris pH 8.0, 100 mM NaCl, 250 mM imidazole pH 8.0, 5%  
504 (v/v) glycerol, 2 mM βME) and the protein was eluted with 100% NiNTA B. The eluent  
505 was concentrated in a 10,000 MWCO Amicon Concentrator (Millipore) to <1 mL and  
506 injected onto a Superdex™ 75 10/300 GL Increase size-exclusion column (GE  
507 Healthcare) equilibrated in gel filtration buffer (20mM Tris pH 8.5, 100 mM NaCl, 50 mM  
508 Ammonium Sulfate and 0.5 mM tris(2-carboxyethyl) phosphine (TCEP)). Following size  
509 exclusion, the protein was concentrated, frozen and stored at -80°C.

510

### 511 *Phosphorylation analysis*

512 For the dose–response phosphorylation of p110γ, p110/p84, and p110/p101, each  
513 protein or complex (750nM) was mixed with ATP (200 µM), GFB (20mM Tris pH 8.5, 100  
514 mM NaCl, 50 mM Ammonium Sulfate and 0.5 mM TCEP), MgCl<sub>2</sub>(20mM) and various  
515 amounts of PKC (4 µg, 800 ng, 160 ng, 32 ng, 6.4 ng, and 0 ng). Reactions were  
516 incubated for three hours on ice and quenched with 50 µL of ice-cold acidic quench buffer  
517 (0.7 M guanidine-HCl, 1% formic acid). followed by immediate freezing using liquid  
518 nitrogen and storage at –80 °C.

519 For the experiment studying the effect of nanobody on phosphorylation, p110 $\gamma$  or  
520 p110/p101, (500nM) was mixed with ATP (1 mM), GFB (20mM Tris pH 8.5, 100 mM NaCl,  
521 50 mM Ammonium Sulfate and 0.5 mM TCEP), MgCl<sub>2</sub>(20mM), with nanobody and PKC  
522 present at 1200 nM and 500nM, respectively. Reactions were incubated for one hour at  
523 room temperature and quenched with 54  $\mu$ L of ice-cold acidic quench buffer (0.7 M  
524 guanidine-HCl, 1% formic acid) followed by immediate freezing using liquid nitrogen and  
525 storage at  $-80^{\circ}\text{C}$ .

526 Phosphorylation of all proteins was confirmed using Mass spectrometry and  
527 PEAKS7 analysis. The phosphorylated and non-phosphorylated peptide ratios were  
528 determined by generating extracted ion chromatograms for each peptide using their  
529 molecular formula and charge state in the Bruker Compass Data Analysis software. The  
530 area under each extracted curve was then extracted. The full MS quantification of each  
531 of the phosphorylated and non-phosphorylated peptide is provided in the source data.

532

533

#### 534 *Lipid vesicle preparation for kinase activity assays*

535 Lipid vesicles containing 5% brain phosphatidylinositol 4,5- bisphosphate (PIP<sub>2</sub>), and  
536 95% brain phosphatidylserine (PS), were prepared by mixing the lipids solutions in  
537 organic solvent. The solvent was evaporated in a stream of argon following which the lipid  
538 film was desiccated in a vacuum for 45 minutes. The lipids were resuspended in lipid  
539 buffer (20 mM HEPES pH 7.0, 100 mM NaCl and 10 % glycerol) and the solution was  
540 vortexed for 5 minutes followed by sonication for 15 minutes. The vesicles were then  
541 subjected to ten freeze thaw cycles and extruded 11 times through a 100-nm filter (T&T  
542 Scientific: TT-002-0010). The extruded vesicles were sub-aliquoted and stored at  $-80^{\circ}\text{C}$ .  
543 Final vesicle concentration was 2 mg/mL.

544

#### 545 *Kinase Assays*

546 All kinase assays were done using Transcreener ADP2 Fluorescence Intensity (FI)  
547 assays (Bellbrook labs) which measures ADP production. All assays used super-lipid  
548 vesicles [5% phosphatidylinositol 4,5-bisphosphate (PI(4,5)P<sub>2</sub>), and 95%

549 phosphatidylserine (PS)] at final concentration of 0.5 mg/mL, and ATP at a final  
550 concentration of 100  $\mu$ M.

551 For assays measuring the inhibition by nanobody, 4X kinase (final concentration:  
552 330 nM for p110 $\gamma$ , 300nM for p110 $\gamma$ /p84 and 12nM for p110 $\gamma$ /p101) was mixed with  
553 varying 4X concentrations of nanobody (final concentration: 2 $\mu$ M – 2.7nM) or kinase  
554 buffer (20mM HEPES pH 7.5, 100mM NaCl, 3mM MgCl<sub>2</sub>, 0.03% CHAPS, 2mM TCEP,  
555 and 1mM EGTA) and allowed to sit on ice for 15 minutes. 2  $\mu$ l of protein mix was mixed  
556 with 2  $\mu$ l of lipid solution containing G $\beta\gamma$  (1 $\mu$ M final concentration), ATP (100  $\mu$ M), Super  
557 lipid (0.5mg/ml final concentration), and lipid buffer (25mM HEPES pH 7, 5% Glycerol,  
558 and 100mM NaCl) and incubated at room temperature for 60 minutes.

559 For assays comparing the difference in activation between phosphorylated and non-  
560 phosphorylated p110 $\gamma$ , 2X kinase (final concentrations: 1 $\mu$ M – 12.3nM) was mixed with  
561 2X lipid solutions containing ATP (100  $\mu$ M), and lipid buffer and either nanobody (3  $\mu$ M  
562 final concentration), Super lipid (0.5mg/ml final concentration) or both nanobody and lipid.  
563 The reaction was incubated at room temperature for 60 minutes.

564 After the 60-minute incubation, all reactions were stopped with 4  $\mu$ L of 2X stop and  
565 detect solution containing Stop and Detect buffer (20mM HEPES,0.02% Brij-35, 400mM  
566 40mM EDTA pH 7.5), 8 nM ADP Alexa Fluor 594 Tracer and 93.7  $\mu$ g/mL ADP2 Antibody  
567 IRDye QC-1, covered and incubated at room temperature for 1 hr before reading the  
568 fluorescence. The fluorescence intensity was measured using a SpectraMax M5 plate  
569 reader at excitation 590 nm and emission 620 nm. All data was normalized against the  
570 appropriate measurements obtained for 100  $\mu$ M ATP and 100  $\mu$ M ADP with no kinase.  
571 The percent ATP turnover was interpolated using a standard curve (0.1-100  $\mu$ M ADP).  
572 Interpolated values were then used to calculate the specific activity of the enzyme.

573

#### 574 *Biolayer interferometry*

575 All Biolayer interferometry experiments were performed using the Octet K2 (Fortebio Inc.).  
576 When comparing nanobody binding to each complex, His-tagged nanobody was  
577 immobilized on an Anti-Penta-His biosensor for 600s, and the sensor was dipped into  
578 solutions of varying concentrations of p110 $\gamma$ , p110p84, and p110p101 (50 nM – 1.9 nM)

579 for 600s followed by a 1200s dissociation step in Octet Buffer (20 mM tris pH 8.5, 100  
580 mM NaCl, 50 mM ammonium sulfate, 0.1% bovine serum albumin, and 0.02% Tween  
581 20). Experiments comparing class IA PI3K versus class IB PI3K used 500 nM nanobody  
582 loaded on the Octet tip, and 50 nM of PI3Ks. When comparing nanobody binding to  
583 phosphorylated and unphosphorylated p110 $\gamma$ , His-tagged nanobody was immobilized on  
584 an Anti-Penta-His biosensor for 600 s, and the sensor was dipped into solutions of either  
585 phosphorylated or non-phosphorylated p110 $\gamma$  at a final concentration of 25 nM for 600s  
586 followed by a dissociation step for 600s. The average  $K_D$  (dissociation constant) was  
587 calculated from the binding curves based on their global fit to a 1:1 binding model.

588

### 589 *Supported lipid bilayer TIRF microscopy experiments*

590 The membrane binding dynamics of Dy647-p84-p110 $\gamma$  were measured in the  
591 absence and presence of nanobody 7 (NB7) using TIRF microscopy. As previously  
592 described (Rathinaswamy et al., 2023), supported lipid bilayers were formed using 50 nm  
593 extruded small unilamellar vesicles (SUVs) containing the following lipids: 1,2-dioleoyl-  
594 sn-glycero-3-phosphocholine (18:1 DOPC, Avanti # 850375C), 1,2-dioleoyl-sn-glycero-3-  
595 phospho-L-serine (18:1 DOPS, Avanti # 840035C), 1,2-dioleoyl-sn-glycero-3-  
596 phosphoethanolamine-N-[4-(p-maleimidomethyl)cyclohexane-carboxamide] (18:1 MCC-  
597 PE, Avanti # 780201C). Lipid compositions reported in figure legends represent the molar  
598 percentage of each lipid species.

599 To create SLBs, a total concentration of 0.25 mM lipids was solvated in 1x PBS  
600 [pH 7.4] and deposited on Piranha etched glass coverslips (25 x 75 mm) adhered to an  
601 IBIDI chamber. After a 30-minute incubation, membranes were washed with 4 mL of 1x  
602 PBS [pH 7.4] and then blocked for 10 minutes with 1 mg/mL beta casein (Thermo  
603 FisherSci, Cat# 37528) in 1x PBS [pH 7.4] (Corning, Cat# 46-013-CM). To conjugate H-  
604 Ras to maleimide lipids (MCC-PE), blocked membranes were incubated with 30  $\mu$ M H-  
605 Ras(GDP) in buffer containing 1x PBS [pH 7.4], 1 mM MgCl<sub>2</sub>, 50  $\mu$ M GDP, and 0.1 mM  
606 TCEP for 2 hours. The membrane conjugation reaction was terminated after 2 hours with  
607 1x PBS [pH 7.4] containing 5 mM  $\beta$ -mercaptoethanol ( $\beta$ ME). Membranes were then

608 washed and stored in 1x PBS [pH 7.4] until performing the TIRF-M membrane binding  
609 experiments. H-Ras was purified as previously described (Rathinaswamy et al., 2023).

610 To perform the TIRF-M membrane binding assays, 200 nM farnesyl-*Gβγ* was  
611 equilibrated into the supported membranes for 30 minutes. In parallel, nucleotide  
612 exchange of H-Ras(GDP) was performed by adding 50 nM guanine nucleotide exchange  
613 factor (SosCat) in 1x PBS [pH 7.4], 1 mM MgCl<sub>2</sub>, 50 μM GDP. To measure membrane  
614 binding, Dy647-p84-p110γ was diluted into the following buffer: 20 mM HEPES [pH 7.0],  
615 150 mM NaCl, 50 μM GTP, 1 mM ATP, 5 mM MgCl<sub>2</sub>, 0.5 mM EGTA, 20 mM glucose, 200  
616 μg/mL beta casein (ThermoScientific, Cat# 37528), 20 mM BME, 320 μg/mL glucose  
617 oxidase (Serva, #22780.01 *Aspergillus niger*), 50 μg/mL catalase (Sigma, #C40-100MG  
618 Bovine Liver), and 2 mM Trolox. Trolox was prepared as previously described (Hansen  
619 et al., 2019). Perishable reagents (i.e. glucose oxidase, catalase, and Trolox) were added  
620 10 minutes before image acquisition.

621 TIRF-M experiments were performed using an inverted Nikon Ti2 microscope with  
622 a 100x Nikon (1.49 NA) oil immersion objective. The x-axis and y-axis positions were  
623 controlled using a Nikon motorized stage. Dy647-p84-p110γ was excited with a 637 nm  
624 diode laser (OBIS laser diode, Coherent Inc. Santa Clara, CA) controlled with an acousto-  
625 optic tunable filter (AOTF) and laser launch built by Vortran (Sacramento, CA). The power  
626 output measured through the objective for single particle imaging was 1-3 mW. Excitation  
627 light passing through quad multi-pass dichroic filter cube (Semrock). Fluorescence  
628 emission passed through Nikon emission filter wheel containing the following 25 mm  
629 ET700/75M emission filters (Semrock) before being detected on iXion Life 897 EMCCD  
630 camera (Andor Technology Ltd., UK). All TIRF-M experiments were performed at room  
631 temperature (23°C). Microscope hardware was controlled using Nikon NIS elements.  
632 Data analysis was performed using ImageJ/Fiji and Prism graphing program.

633

### 634 *Cryo-EM Sample Preparation and Data Collection*

635 3 μL of purified nanobody-bound p110γ at 0.45 mg/ml was adsorbed onto C-Flat 2/2-T  
636 grids that were glow discharged for 25 s at 15 mA. Grids were then plunged into liquid  
637 ethane using a Vitrobot Mark IV (Thermo Fisher Scientific) with the following settings: -5

638 blot force, 1.5 s blot time, 100% humidity and 4 °C. Vitrified specimens were screened for  
639 ice and particle quality at the UBC High resolution macromolecular electron microscopy  
640 (HRMEM) facility using a 200-kV Glacios transmission electron microscope equipped with  
641 a Falcon 3EC direct electron detector (DED). Clipped grids were sent to the Pacific  
642 Northwest Cryo-EM Center (PNCC) where 7,322 movies were collected using a Titan  
643 Krios equipped with a Gatan K3 DED and a BioQuantum K3 energy filter with a slit width  
644 of 20 eV. The movies were collected at a physical pixel size of 0.830 Å/pix and a total  
645 dose of 50e<sup>-</sup>/Å<sup>2</sup> over 50 frames.

646

#### 647 *Cryo-EM image analysis*

648 The data were processed using cryoSPARC v.3.3.2 (Punjani et al., 2017). The  
649 movies were pre-processed by patch motion correction using default settings except  
650 Fourier-cropping by a factor of 2, followed by patch CTF estimation using default settings.  
651 A 3D map of PI3K p110 $\gamma$ -p101 complex (EMD-23808) was used to create 2D projections  
652 for use as templates to auto-pick 1,463,553 particles. Particles were extracted with a box  
653 size of 380 pixels, Fourier cropped to a box size of 96 pixels and subjected to 2D  
654 classification. After discarding classes with obvious noise and no features, 795,162  
655 particles were used for multiple rounds of *ab initio* reconstruction and heterogeneous  
656 refinement using 4 or 5 classes. 365,178 particles, which generated the two best 3D  
657 reconstruction, were used to carry out Per-particle local-motion correction with 760 pixels  
658 box size later downsized to 380 pixels followed by several rounds of *ab initio*  
659 reconstruction and heterogeneous refinement using 3 or 5 classes. 149,603 from best  
660 class were further refined by homogeneous refinement and a final Non-Uniform (NU)-  
661 refinement which generated a reconstruction with an overall resolution of 3.02 Å based  
662 on the Fourier shell correlation (FSC) 0.143 criterion.

663

#### 664 *Building the structural model of p110 $\gamma$ -NB7*

665 The previous structural model of full length p110 $\gamma$  from the complex of p110 $\gamma$ -  
666 p101(PDB: 7MEZ) (Rathinaswamy et al., 2021a) was fit into the map using Chimera

667 (Pettersen et al., 2004). A model of the nanobody was generated using Alphafold2 using  
668 the Colabfold v1.5.2 server (Mirdita et al., 2022). The CDR loops were removed from this  
669 initial model, and the remaining nanobody was fit into the map using Chimera. The final  
670 structure was built by iterative rounds of automated model building in Phenix, manual  
671 model building in COOT (Emsley et al., 2010), and refinement in  
672 Phenix.real\_space\_refine using realspace, rigid body, and adp refinement with tight  
673 secondary structure restraints (Afonine et al., 2012). This allowed for unambiguous  
674 building of the CDRs of the nanobody, and their interface with p110 $\gamma$ . The full refinement  
675 and validation statistics are shown in Supplemental table 1.

676

### 677 *Hydrogen Deuterium eXchange Mass Spectrometry*

678 Exchange reactions to assess differences in p110 $\gamma$  upon phosphorylation were  
679 carried out at 20°C in 10  $\mu$ L volumes with final concentrations of 1.6  $\mu$ M for both apo and  
680 phosphorylated p110 $\gamma$ . A total of two conditions were assessed: p110 $\gamma$  apo and PKC $\beta$   
681 phosphorylated p110 $\gamma$ . The hydrogen-deuterium exchange reaction was initiated by the  
682 addition of 8  $\mu$ L D<sub>2</sub>O buffer (94.3% D<sub>2</sub>O, 100 mM NaCl, 20 mM HEPES pH 7.5) to the 2  
683  $\mu$ L protein for a final D<sub>2</sub>O concentration of 75.4%. Exchange was carried out over five  
684 time points (3s on ice, and 3s, 30s, 300s and 3000s at 20°C) and the reaction was  
685 quenched with addition of 60  $\mu$ L of ice-cold acidic quench buffer (0.7 M guanidine-HCl,  
686 1% formic acid). After quenching, samples were immediately frozen in liquid nitrogen and  
687 stored at -80°C. All reactions were carried out in triplicate.

688

689 *Protein Digestion and MS/MS Data Collection:* Protein samples were rapidly  
690 thawed and injected onto an integrated fluidics system containing a HDx-3 PAL liquid  
691 handling robot and climate-controlled chromatography system (LEAP Technologies), a  
692 Dionex Ultimate 3000 UHPLC system, as well as an Impact HD QTOF Mass spectrometer  
693 (Bruker). The protein was run over two immobilized pepsin columns (Applied Biosystems;  
694 Poroszyme™ Immobilized Pepsin Cartridge, 2.1 mm x 30 mm; Thermo-Fisher 2-3131-  
695 00; at 10°C and 2°C respectively) at 200  $\mu$ L/min for 3 minutes. The resulting peptides  
696 were collected and desalted on a C18 trap column [Acquity UPLC BEH C18 1.7 mm

697 column (2.1 x 5 mm); Waters 186003975]. The trap was subsequently eluted in line with  
698 an ACQUITY 1.7  $\mu\text{m}$  particle, 100 x 1 mm<sup>2</sup> C18 UPLC column (Waters 186002352), using  
699 a gradient of 3-35% B (buffer A, 0.1% formic acid; buffer B, 100% acetonitrile) over 11  
700 min immediately followed by a gradient of 35-80% B over 5 minutes. MS experiments  
701 acquired over a mass range from 150 to 2200 mass/charge ratio (m/z) using an  
702 electrospray ionization source operated at a temperature of 200°C and a spray voltage of  
703 4.5 kV.

704

705 *Peptide Identification:* Peptides were identified using data-dependent acquisition  
706 following tandem MS/MS experiments (0.5 s precursor scan from 150-2000 m/z; twelve  
707 0.25 s fragment scans from 150-2000 m/z). MS/MS datasets were analyzed using  
708 PEAKS7 (PEAKS), and a false discovery rate was set at 0.1% using a database of purified  
709 proteins and known contaminants. Same approach was used to identify phosphorylated  
710 and non-phosphorylated peptides for our in-vitro phosphorylation experiments, with  
711 variable phosphorylation of STY residues was added to the search. The search  
712 parameters were set with a precursor tolerance of 20 parts per million, fragment mass  
713 error 0.02 Da, and charge states from 1 to 8, with a selection criterion of peptides that  
714 had a  $-10\log P$  score of  $>24.03$  for phosphorylated and  $>23.05$  for non-phosphorylated.  
715 The MS/MS spectra of the PKC phosphorylated peptides are included in Fig S3.

716

717 *Mass Analysis of Peptide Centroids and Measurement of Deuterium Incorporation:*  
718 HD-Examiner Software (Sierra Analytics) was used to automatically calculate the level of  
719 deuterium incorporation into each peptide. All peptides were manually inspected for  
720 correct charge state, correct retention time, and appropriate selection of isotopic  
721 distribution. Deuteration levels were calculated using the centroid of the experimental  
722 isotope clusters. HDX-MS results are presented with no correction for back exchange  
723 shown in the Source data, with the only correction being applied correcting for the  
724 deuterium oxide percentage of the buffer used in the exchange (75.4%). Changes in any  
725 peptide at any time point greater than specified cut-offs (5% and 0.45 Da) and with an  
726 unpaired, two-tailed t-test value of  $p < 0.01$  was considered significant. A number of

727 peptides in the helical domain showed isotope distributions consistent with EX1 H/D  
728 exchange. Attempts to define the relative percentages of each population using  
729 HDExaminer were extremely noisy, so representative EX1 profiles are shown in Fig. 3C.  
730 The raw peptide deuterium incorporation graphs for a selection of peptides with significant  
731 differences are shown in Fig. 4D, with the raw data for all analysed peptides in the source  
732 data. To allow for visualization of differences across all peptides, we utilized number of  
733 deuterium difference (#D) plots (Fig. 4B). These plots show the total difference in  
734 deuterium incorporation over the entire H/D exchange time course, with each point  
735 indicating a single peptide. The data analysis statistics for all HDX-MS experiments are  
736 in Supplemental Table 2 according to the guidelines of (Masson et al., 2019). The mass  
737 spectrometry proteomics data have been deposited to the ProteomeXchange Consortium  
738 via the PRIDE partner repository (Perez-Riverol et al., 2022) with the dataset identifier  
739 PXD040765.

740

## 741 **References**

- 742 Afonine PV, Grosse-Kunstleve RW, Echols N, Headd JJ, Moriarty NW, Mustyakimov M,  
743 Terwilliger TC, Urzhumtsev A, Zwart PH, Adams PD. 2012. Towards automated  
744 crystallographic structure refinement with phenix.refine. *Acta Crystallogr D Biol*  
745 *Crystallogr* **68**:352–367. doi:10.1107/S0907444912001308
- 746 Angulo I, Vadas O, Garçon F, Banham-Hall E, Plagnol V, Leahy TR, Baxendale H,  
747 Coulter T, Curtis J, Wu C, Blake-Palmer K, Perisic O, Smyth D, Maes M, Fiddler  
748 C, Juss J, Cilliers D, Markelj G, Chandra A, Farmer G, Kielkowska A, Clark J,  
749 Kracker S, Debré M, Picard C, Pellier I, Jabado N, Morris JA, Barcenas-Morales  
750 G, Fischer A, Stephens L, Hawkins P, Barrett JC, Abinun M, Clatworthy M,  
751 Durandy A, Doffinger R, Chilvers ER, Cant AJ, Kumararatne D, Okkenhaug K,  
752 Williams RL, Condliffe A, Nejentsev S. 2013. Phosphoinositide 3-kinase  $\delta$  gene  
753 mutation predisposes to respiratory infection and airway damage. *Science*  
754 **342**:866–871. doi:10.1126/science.1243292
- 755 Becattini B, Marone R, Zani F, Arsenijevic D, Seydoux J, Montani J, Dulloo A, Thorens  
756 B, Preitner F, Wymann M, Solinas G. 2011. PI3Kgamma within a  
757 nonhematopoietic cell type negatively regulates diet-induced thermogenesis and  
758 promotes obesity and insulin resistance. *Proc Natl Acad Sci USA* **108**:E854-63.  
759 doi:10.1073/pnas.1106698108/-/DCSupplemental
- 760 Bell K, Sunose M, Ellard K, Cansfield A, Taylor J, Miller W, Ramsden N, Bergamini G,  
761 Neubauer G. 2012. SAR studies around a series of triazolopyridines as potent  
762 and selective PI3K $\gamma$  inhibitors. *Bioorg Med Chem Lett* **22**:5257–5263.  
763 doi:10.1016/j.bmcl.2012.06.049

- 764 Bohnacker T, Marone R, Collmann E, Calvez R, Hirsch E, Wymann M. 2009.  
765 PI3Kgamma adaptor subunits define coupling to degranulation and cell motility  
766 by distinct PtdIns(3,4,5)P3 pools in mast cells. *Sci Signal* **2**:ra27.  
767 doi:10.1126/scisignal.2000259
- 768 Bohnacker T, Prota AE, Beaufils F, Burke JE, Melone A, Inglis AJ, Rageot D, Sele AM,  
769 Cmiljanovic V, Cmiljanovic N, Bargsten K, Aher A, Akhmanova A, Díaz JF,  
770 Fabbro D, Zvelebil M, Williams RL, Steinmetz MO, Wymann MP. 2017.  
771 Deconvolution of Buparlisib's mechanism of action defines specific PI3K and  
772 tubulin inhibitors for therapeutic intervention. *Nat Commun* **8**:14683.  
773 doi:10.1038/ncomms14683
- 774 Breasson L, Becattini B, Sardi C, Molinaro A, Zani F, Marone R, Botindari F,  
775 Bousquenaud M, Ruegg C, Wymann MP, Solinas G. 2017. PI3Kγ activity in  
776 leukocytes promotes adipose tissue inflammation and early-onset insulin  
777 resistance during obesity. *Sci Signal* **10**:eaaf2969. doi:10.1126/scisignal.aaf2969
- 778 Burke JE. 2018. Structural Basis for Regulation of Phosphoinositide Kinases and Their  
779 Involvement in Human Disease. *Mol Cell* **71**:653–673.  
780 doi:10.1016/j.molcel.2018.08.005
- 781 Burke JE, Perisic O, Masson GR, Vadas O, Williams RL. 2012. Oncogenic mutations  
782 mimic and enhance dynamic events in the natural activation of phosphoinositide  
783 3-kinase p110α (PIK3CA). *Proc Natl Acad Sci USA* **109**:15259–15264.  
784 doi:10.1073/pnas.1205508109
- 785 Burke JE, Vadas O, Berndt A, Finegan T, Perisic O, Williams RL. 2011. Dynamics of the  
786 phosphoinositide 3-kinase p110δ interaction with p85α and membranes reveals  
787 aspects of regulation distinct from p110α. *Structure* **19**:1127–1137.  
788 doi:10.1016/j.str.2011.06.003
- 789 Burke JE, Williams RL. 2015. Synergy in activating class I PI3Ks. *Trends in Biochemical*  
790 *Sciences* **40**:88–100. doi:10.1016/j.tibs.2014.12.003
- 791 Burke JE, Williams RL. 2013. Dynamic steps in receptor tyrosine kinase mediated  
792 activation of class IA phosphoinositide 3-kinases (PI3K) captured by H/D  
793 exchange (HDX-MS). *Adv Biol Regul* **53**:97–110. doi:10.1016/j.jbior.2012.09.005
- 794 Campa CC, Silva RL, Margaria JP, Pirali T, Mattos MS, Kraemer LR, Reis DC, Grosa  
795 G, Copperi F, Dalmarco EM, Lima-Júnior RCP, Aprile S, Sala V, Dal Bello F,  
796 Prado DS, Alves-Filho JC, Medana C, Cassali GD, Tron GC, Teixeira MM,  
797 Ciraolo E, Russo RC, Hirsch E. 2018. Inhalation of the prodrug PI3K inhibitor  
798 CL27c improves lung function in asthma and fibrosis. *Nat Commun* **9**:5232–16.  
799 doi:10.1038/s41467-018-07698-6
- 800 Camps M, Rückle T, Ji H, Ardisson V, Rintelen F, Shaw J, Ferrandi C, Chabert C,  
801 Gillieron C, Françon B, Martin T, Gretener D, Perrin D, Leroy D, Vitte P-A, Hirsch  
802 E, Wymann MP, Cirillo R, Schwarz MK, Rommel C. 2005. Blockade of  
803 PI3Kgamma suppresses joint inflammation and damage in mouse models of  
804 rheumatoid arthritis. *Nat Med* **11**:936–943. doi:10.1038/nm1284
- 805 De Henau O, Rausch M, Winkler D, Campesato LF, Liu C, Cymerman DH, Budhu S,  
806 Ghosh A, Pink M, Tchaicha J, Douglas M, Tibbitts T, Sharma S, Proctor J,  
807 Kosmider N, White K, Stern H, Soglia J, Adams J, Palombella VJ, McGovern K,

- 808 Kutok JL, Wolchok JD, Merghoub T. 2016. Overcoming resistance to checkpoint  
809 blockade therapy by targeting PI3K $\gamma$  in myeloid cells. *Nature* **539**:443–447.  
810 doi:10.1038/nature20554
- 811 Deladeriere A, Gambardella L, Pan D, Anderson KE, Hawkins PT, Stephens LR. 2015.  
812 The regulatory subunits of PI3K $\gamma$  control distinct neutrophil responses. *Sci Signal*  
813 **8**:ra8. doi:10.1126/scisignal.2005564
- 814 Dornan GL, Siempelkamp BD, Jenkins ML, Vadas O, Lucas CL, Burke JE. 2017.  
815 Conformational disruption of PI3K $\delta$  regulation by immunodeficiency mutations in  
816 PIK3CD and PIK3R1. *Proc Natl Acad Sci USA* **114**:1982–1987.  
817 doi:10.1073/pnas.1617244114
- 818 Emsley P, Lohkamp B, Scott WG, Cowtan K. 2010. Features and development of Coot.  
819 *Acta Crystallogr D Biol Crystallogr* **66**:486–501.  
820 doi:10.1107/S0907444910007493
- 821 Evans CA, Liu T, Lescarbeau A, Nair SJ, Grenier L, Pradeilles JA, Glenadel Q, Tibbitts  
822 T, Rowley AM, DiNitto JP, Brophy EE, O’Hearn EL, Ali JA, Winkler DG, Goldstein  
823 SI, O’Hearn P, Martin CM, Hoyt JG, Soglia JR, Cheung C, Pink MM, Proctor JL,  
824 Palombella VJ, Tremblay MR, Castro AC. 2016. Discovery of a Selective  
825 Phosphoinositide-3-Kinase (PI3K)- $\gamma$  Inhibitor (IPI-549) as an Immuno-Oncology  
826 Clinical Candidate. *ACS Med Chem Lett* **7**:862–867.  
827 doi:10.1021/acsmchemlett.6b00238
- 828 Gangadhara G, Dahl G, Bohnacker T, Rae R, Gunnarsson J, Blaho S, Öster L,  
829 Lindmark H, Karabelas K, Pemberton N, Tyrchan C, Mogemark M, Wymann MP,  
830 Williams RL, Perry MWD, Papavoine T, Petersen J. 2019. A class of highly  
831 selective inhibitors bind to an active state of PI3K $\gamma$ . *Nature Chemical Biology*  
832 **15**:348–357. doi:10.1038/s41589-018-0215-0
- 833 Hansen SD, Huang WYC, Lee YK, Bieling P, Christensen SM, Groves JT. 2019.  
834 Stochastic geometry sensing and polarization in a lipid kinase-phosphatase  
835 competitive reaction. *Proc Natl Acad Sci U S A* **116**:15013–15022.  
836 doi:10.1073/pnas.1901744116
- 837 Hawkins PT, Stephens LR. 2015. PI3K signalling in inflammation. *Biochim Biophys Acta*  
838 **1851**:882–897. doi:10.1016/j.bbali.2014.12.006
- 839 Jenkins ML, Ranga-Prasad H, Parson MAH, Harris NJ, Rathinaswamy MK, Burke JE.  
840 2023. Oncogenic mutations of PIK3CA lead to increased membrane recruitment  
841 driven by reorientation of the ABD, p85 and C-terminus. *Nat Commun* **14**:181.  
842 doi:10.1038/s41467-023-35789-6
- 843 Jin JR, Gogvadze E, Xavier AR, Bohnacker T, Voelzmann J, Wymann MP. 2020. PI3K $\gamma$   
844 Regulatory Protein p84 Determines Mast Cell Sensitivity to Ras Inhibition-Moving  
845 Towards Cell Specific PI3K Targeting? *Front Immunol* **11**:585070.  
846 doi:10.3389/fimmu.2020.585070
- 847 Johannessen CM, Boehm JS, Kim SY, Thomas SR, Wardwell L, Johnson LA, Emery  
848 CM, Stransky N, Cogdill AP, Barretina J, Caponigro G, Hieronymus H, Murray  
849 RR, Salehi-Ashtiani K, Hill DE, Vidal M, Zhao JJ, Yang X, Alkan O, Kim S, Harris  
850 JL, Wilson CJ, Myer VE, Finan PM, Root DE, Roberts TM, Golub T, Flaherty KT,  
851 Dummer R, Weber BL, Sellers WR, Schlegel R, Wargo JA, Hahn WC, Garraway

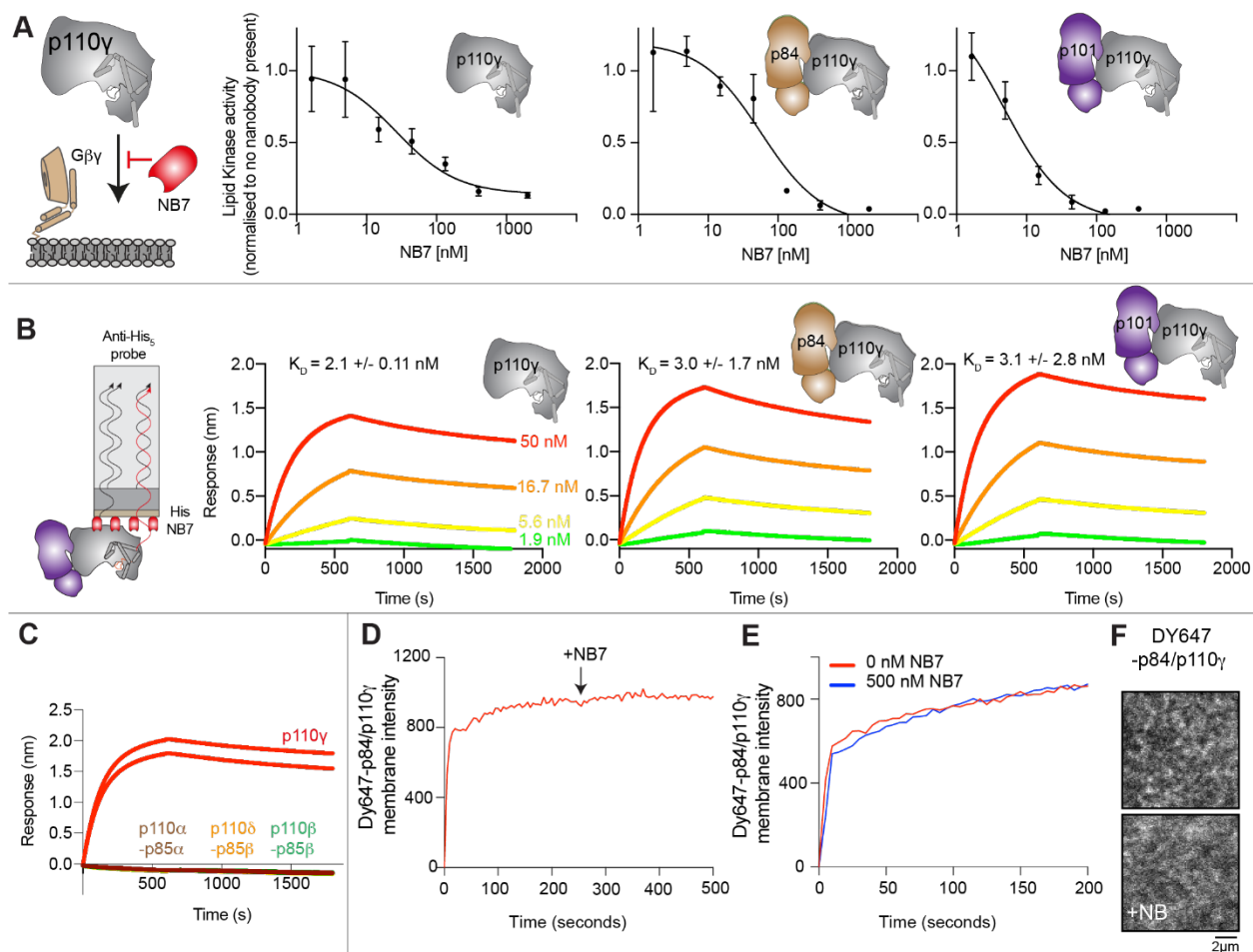
- 852 LA. 2010. COT drives resistance to RAF inhibition through MAP kinase pathway  
853 reactivation. *Nature* **468**:968–972. doi:10.1038/nature09627
- 854 Kaneda MM, Cappello P, Nguyen AV, Ralainirina N, Hardamon CR, Foubert P, Schmid  
855 MC, Sun P, Mose E, Bouvet M, Lowy AM, Valasek MA, Sasik R, Novelli F, Hirsch  
856 E, Varner JA. 2016a. Macrophage PI3K $\gamma$  Drives Pancreatic Ductal  
857 Adenocarcinoma Progression. *Cancer Discov* **6**:870–885. doi:10.1158/2159-  
858 8290.CD-15-1346
- 859 Kaneda MM, Messer KS, Ralainirina N, Li H, Leem CJ, Gorjestani S, Woo G, Nguyen  
860 AV, Figueiredo CC, Foubert P, Schmid MC, Pink M, Winkler DG, Rausch M,  
861 Palombella VJ, Kutok J, McGovern K, Frazer KA, Wu X, Karin M, Sasik R, Cohen  
862 EEW, Varner JA. 2016b. PI3K $\gamma$  is a molecular switch that controls immune  
863 suppression. *Nature* **539**:437–442. doi:10.1038/nature19834
- 864 Kurig B, Shymanets A, Bohnacker T, Prajwal, Brock C, Ahmadian MR, Schaefer M,  
865 Gohla A, Harteneck C, Wymann MP, Jeanclos E, Nürnberg B. 2009. Ras is an  
866 indispensable coregulator of the class IB phosphoinositide 3-kinase  
867 p87/p110 $\gamma$ . *Proc Natl Acad Sci USA* **106**:20312–20317.  
868 doi:10.1073/pnas.0905506106
- 869 Laffargue M, Calvez R, Finan P, Trifilieff A, Barbier M, Altruda F, Hirsch E, Wymann  
870 MP. 2002. Phosphoinositide 3-kinase  $\gamma$  is an essential amplifier of mast  
871 cell function. *Immunity* **16**:441–451.
- 872 Lanahan SM, Wymann MP, Lucas CL. 2022. The role of PI3K $\gamma$  in the immune system:  
873 new insights and translational implications. *Nat Rev Immunol*.  
874 doi:10.1038/s41577-022-00701-8
- 875 Lawrence MS, Stojanov P, Mermel CH, Robinson JT, Garraway LA, Golub TR,  
876 Meyerson M, Gabriel SB, Lander ES, Getz G. 2014. Discovery and saturation  
877 analysis of cancer genes across 21 tumour types. *Nature* **505**:495–501.  
878 doi:10.1038/nature12912
- 879 Li H, Prever L, Hirsch E, Gulluni F. 2021. Targeting PI3K/AKT/mTOR Signaling Pathway  
880 in Breast Cancer. *Cancers (Basel)* **13**:3517. doi:10.3390/cancers13143517
- 881 Li Z, Jiang H, Xie W, Zhang Z, Smrcka AV, Wu D. 2000. Roles of PLC- $\beta$ 2 and - $\beta$ 3  
882 and PI3K $\gamma$  in chemoattractant-mediated signal transduction. *Science*  
883 **287**:1046–1049. doi:10.1126/science.287.5455.1046
- 884 Liu X, Zhou Q, Hart JR, Xu Y, Yang S, Yang D, Vogt PK, Wang M-W. 2022. Cryo-EM  
885 structures of cancer-specific helical and kinase domain mutations of PI3K $\alpha$ . *Proc*  
886 *Natl Acad Sci U S A* **119**:e2215621119. doi:10.1073/pnas.2215621119
- 887 Lucas CL, Kuehn HS, Zhao F, Niemela JE, Deenick EK, Palendira U, Avery DT, Moens  
888 L, Cannons JL, Biancalana M, Stoddard J, Ouyang W, Frucht DM, Rao VK,  
889 Atkinson TP, Agharahimi A, Hussey AA, Folio LR, Olivier KN, Fleisher TA,  
890 Pittaluga S, Holland SM, Cohen JI, Oliveira JB, Tangye SG, Schwartzberg PL,  
891 Lenardo MJ, Uzel G. 2014. Dominant-activating germline mutations in the gene  
892 encoding the PI(3)K catalytic subunit p110 $\delta$  result in T cell senescence and  
893 human immunodeficiency. *Nat Immunol* **15**:88–97. doi:10.1038/ni.2771
- 894 Luo L, Wall AA, Tong SJ, Hung Y, Xiao Z, Tarique AA, Sly PD, Fantino E, Marzolo M-P,  
895 Stow JL. 2018. TLR Crosstalk Activates LRP1 to Recruit Rab8a and PI3K $\gamma$  for

- 896           Suppression of Inflammatory Responses. *Cell Rep* **24**:3033–3044.  
897           doi:10.1016/j.celrep.2018.08.028
- 898 Mandelker D, Gabelli SB, Schmidt-Kittler O, Zhu J, Cheong I, Huang C-H, Kinzler KW,  
899 Vogelstein B, Amzel LM. 2009. A frequent kinase domain mutation that changes  
900 the interaction between PI3Kalpha and the membrane. *Proc Natl Acad Sci USA*  
901 **106**:16996–17001. doi:10.1073/pnas.0908444106
- 902 Masson GR, Burke JE, Ahn NG, Anand GS, Borchers C, Brier S, Bou-Assaf GM, Engen  
903 JR, Englander SW, Faber J, Garlish R, Griffin PR, Gross ML, Guttman M,  
904 Hamuro Y, Heck AJR, Houde D, Iacob RE, Jørgensen TJD, Kaltashov IA,  
905 Klinman JP, Konermann L, Man P, Mayne L, Pascal BD, Reichmann D, Skehel  
906 M, Snijder J, Strutzenberg TS, Underbakke ES, Wagner C, Wales TE, Walters  
907 BT, Weis DD, Wilson DJ, Wintrode PL, Zhang Z, Zheng J, Schriemer DC, Rand  
908 KD. 2019. Recommendations for performing, interpreting and reporting hydrogen  
909 deuterium exchange mass spectrometry (HDX-MS) experiments. *Nat Methods*  
910 **16**:595–602. doi:10.1038/s41592-019-0459-y
- 911 Miled N, Yan Y, Hon W-C, Perisic O, Zvelebil M, Inbar Y, Schneidman-Duhovny D,  
912 Wolfson HJ, Backer JM, Williams RL. 2007. Mechanism of two classes of cancer  
913 mutations in the phosphoinositide 3-kinase catalytic subunit. *Science* **317**:239–  
914 242. doi:10.1126/science.1135394
- 915 Mirdita M, Schütze K, Moriwaki Y, Heo L, Ovchinnikov S, Steinegger M. 2022.  
916 ColabFold: making protein folding accessible to all. *Nat Methods* **19**:679–682.  
917 doi:10.1038/s41592-022-01488-1
- 918 Okkenhaug K. 2013. Signaling by the phosphoinositide 3-kinase family in immune cells.  
919 *Annu Rev Immunol* **31**:675–704. doi:10.1146/annurev-immunol-032712-095946
- 920 Pacold ME, Suire S, Perisic O, Lara-Gonzalez S, Davis CT, Walker EH, Hawkins PT,  
921 Stephens L, Eccleston JF, Williams RL. 2000. Crystal structure and functional  
922 analysis of Ras binding to its effector phosphoinositide 3-kinase gamma. *Cell*  
923 **103**:931–943.
- 924 Perez-Riverol Y, Bai J, Bandla C, García-Seisdedos D, Hewapathirana S,  
925 Kamatchinathan S, Kundu DJ, Prakash A, Frericks-Zipper A, Eisenacher M,  
926 Walzer M, Wang S, Brazma A, Vizcaíno JA. 2022. The PRIDE database  
927 resources in 2022: a hub for mass spectrometry-based proteomics evidences.  
928 *Nucleic Acids Res* **50**:D543–D552. doi:10.1093/nar/gkab1038
- 929 Perino A, Ghigo A, Ferrero E, Morello F, Santulli G, Baillie GS, Damilano F, Dunlop AJ,  
930 Pawson C, Walser R, Levi R, Altruda F, Silengo L, Langeberg LK, Neubauer G,  
931 Heymans S, Lembo G, Wymann MP, Wetzker R, Houslay MD, Iaccarino G, Scott  
932 JD, Hirsch E. 2011. Integrating Cardiac PIP(3) and cAMP Signaling through a  
933 PKA Anchoring Function of p110gamma. *Mol Cell* **42**:84–95.  
934 doi:10.1016/j.molcel.2011.01.030
- 935 Pettersen EF, Goddard TD, Huang CC, Couch GS, Greenblatt DM, Meng EC, Ferrin  
936 TE. 2004. UCSF Chimera--a visualization system for exploratory research and  
937 analysis. *J Comput Chem* **25**:1605–1612. doi:10.1002/jcc.20084

- 938 Punjani A, Rubinstein JL, Fleet DJ, Brubaker MA. 2017. cryoSPARC: algorithms for  
939 rapid unsupervised cryo-EM structure determination. *Nat Methods* **14**:290–296.  
940 doi:10.1038/nmeth.4169
- 941 Rathinaswamy MK, Burke JE. 2019. Class I phosphoinositide 3-kinase (PI3K)  
942 regulatory subunits and their roles in signaling and disease. *Adv Biol Regul*  
943 100657. doi:10.1016/j.jbior.2019.100657
- 944 Rathinaswamy MK, Dalwadi U, Fleming KD, Adams C, Stariha JTB, Pardon E, Baek M,  
945 Vadas O, DiMaio F, Steyaert J, Hansen SD, Yip CK, Burke JE. 2021a. Structure  
946 of the phosphoinositide 3-kinase (PI3K) p110 $\gamma$ -p101 complex reveals molecular  
947 mechanism of GPCR activation. *Sci Adv* **7**:eabj4282. doi:10.1126/sciadv.abj4282
- 948 Rathinaswamy MK, Fleming KD, Dalwadi U, Pardon E, Harris NJ, Yip CK, Steyaert J,  
949 Burke JE. 2021b. HDX-MS-optimized approach to characterize nanobodies as  
950 tools for biochemical and structural studies of class IB phosphoinositide 3-  
951 kinases. *Structure* **29**:1371-1381.e6. doi:10.1016/j.str.2021.07.002
- 952 Rathinaswamy MK, Gaieb Z, Fleming KD, Borsari C, Harris NJ, Moeller BE, Wymann  
953 MP, Amaro RE, Burke JE. 2021c. Disease-related mutations in PI3K $\gamma$  disrupt  
954 regulatory C-terminal dynamics and reveal a path to selective inhibitors. *Elife*  
955 **10**:e64691. doi:10.7554/eLife.64691
- 956 Rathinaswamy MK, Jenkins ML, Duwell BR, Zhang X, Harris NJ, Evans JT, Stariha  
957 JTB, Dalwadi U, Fleming KD, Ranga-Prasad H, Yip CK, Williams RL, Hansen  
958 SD, Burke JE. 2023. Molecular basis for differential activation of p101 and p84  
959 complexes of PI3K $\gamma$  by Ras and GPCRs. *Cell Rep* **42**:112172.  
960 doi:10.1016/j.celrep.2023.112172
- 961 Rynkiewicz NK, Anderson KE, Suire S, Collins DM, Karanasios E, Vadas O, Williams R,  
962 Oxley D, Clark J, Stephens LR, Hawkins PT. 2020. G $\beta\gamma$  is a direct regulator of  
963 endogenous p101/p110 $\gamma$  and p84/p110 $\gamma$  PI3K $\gamma$  complexes in mouse neutrophils.  
964 *Sci Signal* **13**:eaaz4003. doi:10.1126/scisignal.aaz4003
- 965 Samuels Y, Wang Z, Bardelli A, Silliman N, Ptak J, Szabo S, Yan H, Gazdar A, Powell  
966 S, Riggins G, Willson J, Markowitz S, Kinzler K, Vogelstein B, Velculescu V.  
967 2004. High frequency of mutations of the PIK3CA gene in human cancers.  
968 *Science* **304**:554. doi:10.1126/science.1096502
- 969 Shymanets A, Prajwal P, Bucher K, Beer-Hammer S, Harteneck C, Nürnberg B. 2013.  
970 p87 and p101 subunits are distinct regulators determining class IB PI3K  
971 specificity. *J Biol Chem* **288**(43):31059–68. doi:10.1074/jbc.M113.508234
- 972 Siempelkamp BD, Rathinaswamy MK, Jenkins ML, Burke JE. 2017. Molecular  
973 mechanism of activation of class IA phosphoinositide 3-kinases (PI3Ks) by  
974 membrane-localized HRas. *J Biol Chem* **292**:12256–12266.  
975 doi:10.1074/jbc.M117.789263
- 976 Stephens LR, Eguinoa A, Erdjument-Bromage H, Lui M, Cooke F, Coadwell J, Smrcka  
977 AS, Thelen M, Cadwallader K, Tempst P, Hawkins PT. 1997. The G $\beta\gamma$  sensitivity  
978 of a PI3K is dependent upon a tightly associated adaptor, p101. *Cell* **89**:105–114.
- 979 Takeda AJ, Maher TJ, Zhang Y, Lanahan SM, Bucklin ML, Compton SR, Tyler PM,  
980 Comrie WA, Matsuda M, Olivier KN, Pittaluga S, McElwee JJ, Long Priel DA,  
981 Kuhns DB, Williams RL, Mustillo PJ, Wymann MP, Koneti Rao V, Lucas CL.

982           2019. Human PI3K $\gamma$  deficiency and its microbiota-dependent mouse model  
983           reveal immunodeficiency and tissue immunopathology. *Nat Commun* **10**:4364–  
984           12. doi:10.1038/s41467-019-12311-5  
985 Vadas O, Dbouk HA, Shymanets A, Perisic O, Burke JE, Abi Saab WF, Khalil BD,  
986           Harteneck C, Bresnick AR, Nürnberg B, Backer JM, Williams RL. 2013.  
987           Molecular determinants of PI3K $\gamma$ -mediated activation downstream of G-protein-  
988           coupled receptors (GPCRs). *Proc Natl Acad Sci U S A* **110**:18862–18867.  
989           doi:10.1073/pnas.1304801110  
990 Vanhaesebroeck B, Perry MWD, Brown JR, André F, Okkenhaug K. 2021. PI3K  
991           inhibitors are finally coming of age. *Nat Rev Drug Discov* **20**:741–769.  
992           doi:10.1038/s41573-021-00209-1  
993 Vasan N, Cantley LC. 2022. At a crossroads: how to translate the roles of PI3K in  
994           oncogenic and metabolic signalling into improvements in cancer therapy. *Nat*  
995           *Rev Clin Oncol*. doi:10.1038/s41571-022-00633-1  
996 Walker EH, Perisic O, Ried C, Stephens L, Williams RL. 1999. Structural insights into  
997           phosphoinositide 3-kinase catalysis and signalling. *Nature* **402**:313–320.  
998           doi:10.1038/46319  
999 Walser R, Burke JE, Gogvadze E, Bohnacker T, Zhang X, Hess D, Küenzi P, Leitges M,  
1000           Hirsch E, Williams RL, Laffargue M, Wymann MP. 2013. PKC $\beta$  phosphorylates  
1001           PI3K $\gamma$  to activate it and release it from GPCR control. *PLoS Biol* **11**:e1001587.  
1002           doi:10.1371/journal.pbio.1001587  
1003 Zhang X, Vadas O, Perisic O, Anderson KE, Clark J, Hawkins PT, Stephens LR,  
1004           Williams RL. 2011. Structure of lipid kinase p110 $\beta$ /p85 $\beta$  elucidates an unusual  
1005           SH2-domain-mediated inhibitory mechanism. *Mol Cell* **41**:567–578.  
1006           doi:10.1016/j.molcel.2011.01.026  
1007  
1008  
1009  
1010  
1011  
1012  
1013  
1014  
1015  
1016  
1017  
1018  
1019

1020 **Figures and Figure Legends**



1021  
1022 **Figure 1. The inhibitory nanobody NB7 binds tightly to all p110γ complexes and inhibits kinase**  
1023 **activity, but does not prevent membrane binding**

1024 **A.** Cartoon schematic depicting nanobody inhibition of activation by lipidated Gβγ (1.5 μM final  
1025 concentration). Lipid kinase assays show a potent inhibition of lipid kinase activity with increasing  
1026 concentrations of NB7 (3-3000 nM) for the different complexes. The protein concentration of p110γ (300  
1027 nM), p110γ-p84 (330 nM) and p110γ-p101 (12 nM) was different due to intrinsic differences of each  
1028 complex to be activated by lipidated Gβγ.

1029 **B.** Association and dissociation curves for the dose response of His-NB7 binding to p110γ, p110γ-p84  
1030 and p110γ-p101 (50 – 1.9 nM) is shown. A cartoon schematic of BLI analysis of the binding of  
1031 immobilized His-NB7 to p110γ is shown on the left. Dissociation constants ( $K_D$ ) were calculated based on  
1032 a global fit to a 1:1 model for the top three concentrations and averaged with error shown.

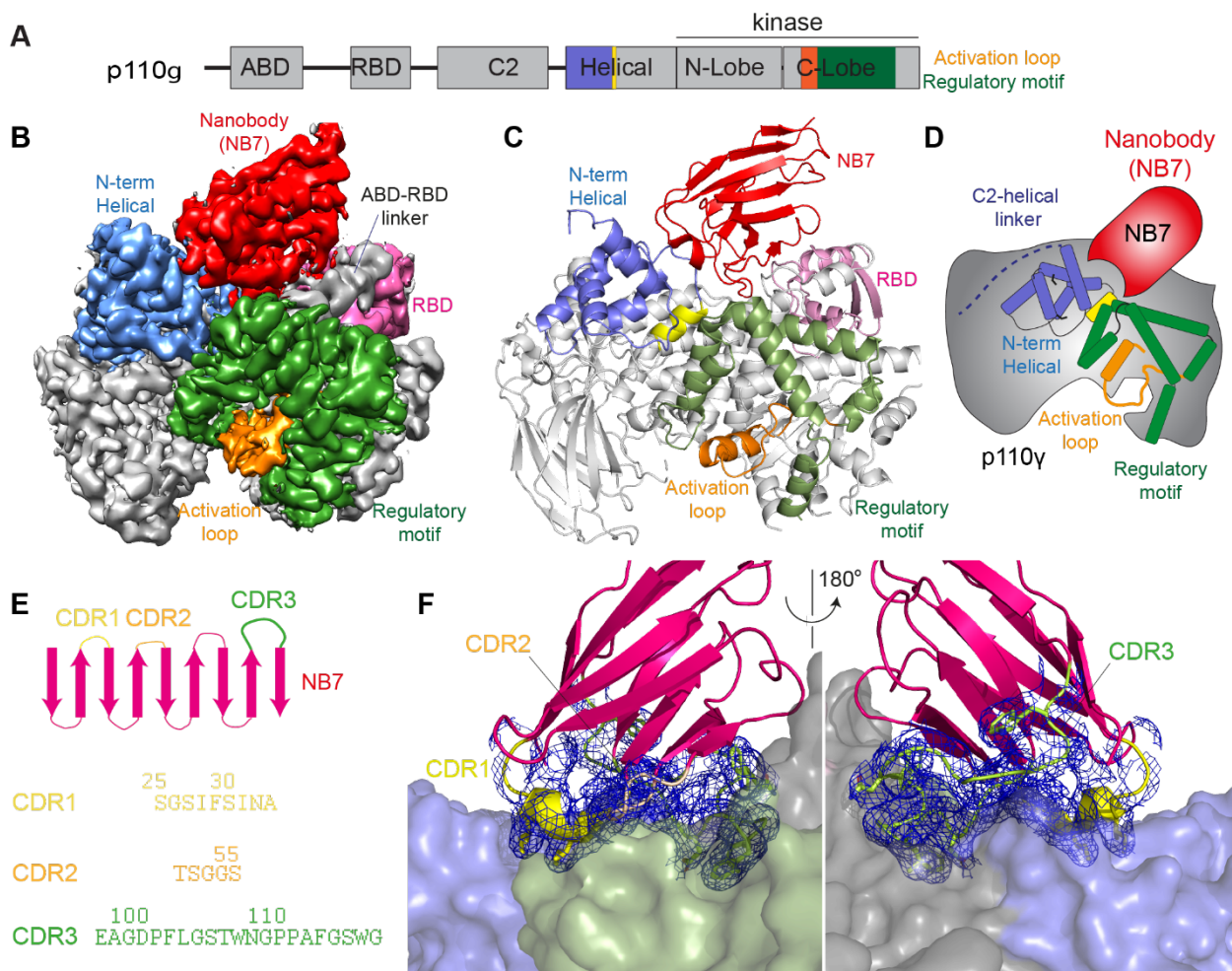
1033 **B.** Association and dissociation curves for His-NB7 binding to p110 $\gamma$ , p110 $\alpha$ -p85 $\alpha$ , p110 $\beta$ -p85 $\beta$ , and  
1034 p110 $\delta$ -p85 $\beta$ . Experiments were performed in duplicate with a final concentration of 50 nM of each class I  
1035 PI3K complex.

1036 **D.** Total Internal Reflection Fluorescence Microscopy (TIRF-M) analysis of the effect of nanobody NB7 on  
1037 PI3K recruitment to supported lipid bilayers containing H-Ras(GTP) and farnesyl-G $\beta\gamma$ . Y647-p84/p110 $\gamma$   
1038 displays rapid equilibration kinetics and is insensitive to the addition of 500 nM nanobody (black arrow,  
1039 250 sec) on supported lipid bilayers containing H-Ras(GTP) and farnesyl-G $\beta\gamma$ .

1040 **E.** Kinetics of 50 nM DY647-p84/p110 $\gamma$  membrane recruitment appears indistinguishable in the absence  
1041 and presence of nanobody. Prior to sample injection, DY647-p84/p110 $\gamma$  was incubated for 10 minutes  
1042 with 500 nM nanobody.

1043 **F.** Representative TIRF-M images showing the localization of 50 nM DY647-p84/p110 $\gamma$  visualized in the  
1044 absence or presence of 500 nM nanobody (+NB7). Membrane composition for panels C-E: 93% DOPC,  
1045 5% DOPS, 2% MCC-PE, Ras(GTP) covalently attached to MCC-PE, and 200 nM farnesyl-G $\beta\gamma$ .

1046  
1047  
1048  
1049  
1050  
1051  
1052  
1053  
1054  
1055  
1056  
1057  
1058  
1059



1060

1061 **Figure 2. Structure of p110γ bound to inhibitory nanobody NB7**

1062 **A.** Domain schematics of p110γ with helical domain (blue), activation loop (orange), and regulatory motif  
1063 (green) of p110 annotated.

1064 **B.** Density map of the p110γ-NB7 complex colored according to the schematic in **A**.

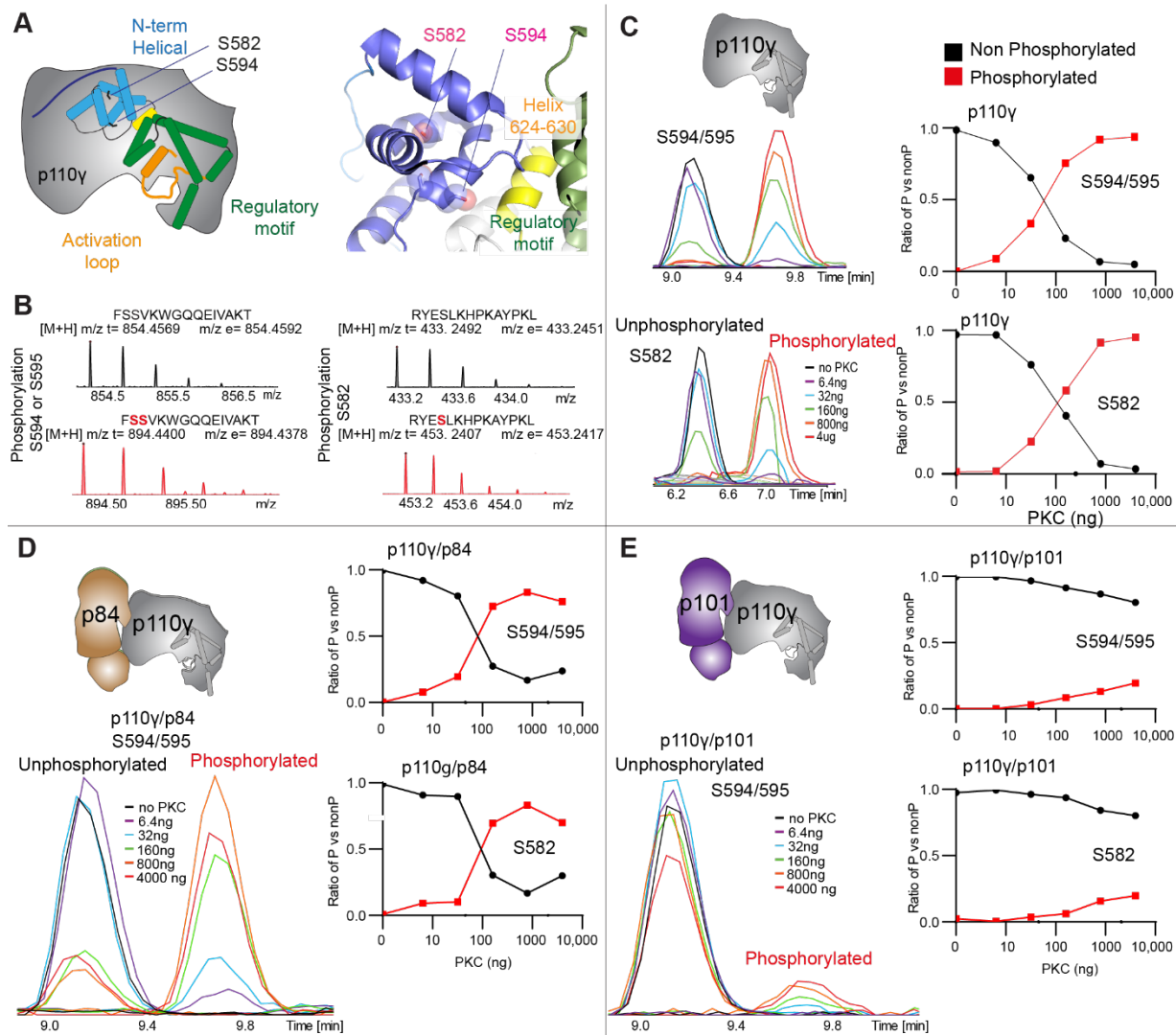
1065 **C.** Cartoon model of the structure of p110γ bound to NB7 colored according to **A**.

1066 **D.** Schematic depicting the key features of p110 and the nanobody binding site, colored according to panel  
1067 **A**.

1068 **E.** Domain schematic of NB7 CDR regions and their sequences.

1069 **F.** Zoom in on the binding interface of NB7, with the CDRs colored as in panel E, and the electron density  
1070 of the CDR regions contoured at 3σ (blue mesh).

1071



1072

1073 **Figure 3. PKC leads to dual phosphorylation of internal sites in the helical domain, with selectivity**  
 1074 **for apo p110 $\gamma$  and p110 $\gamma$ -p84 over p110 $\gamma$ -p101.**

1075 **A.** Putative phosphorylation sites mapped on the structure of p110 $\gamma$  (PDB: 7MEZ) and cartoon schematic.

1076 The regions are colored based on domain schematics featured in Fig 2A.

1077 **B.** Raw MS spectra of the unphosphorylated and phosphorylated peptide for a region spanning 579-592

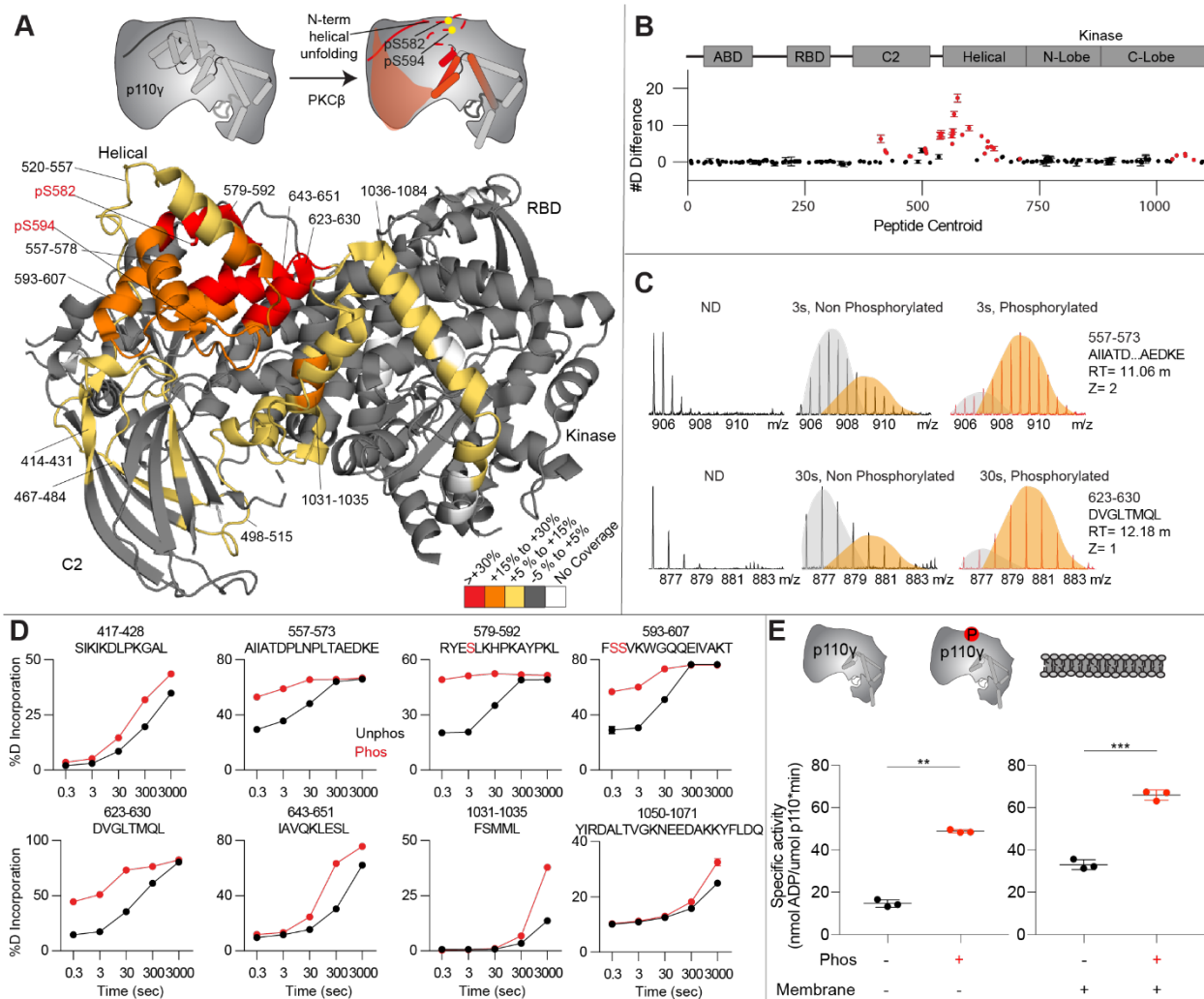
1078 (RYESLKHPKAYPKL) and 593-607 (FSSVKWGQQEIVAKT).

1079 **C-E.** Extracted traces and ratios of the intensity of extracted ion traces of different phosphorylation site

1080 peptides (Top to bottom: S594/S595 and S582) from p110 $\gamma$ , **(D)** p110 $\gamma$ /p84 or **(E)** p110 $\gamma$ /p101 samples

1081 treated with increasing concentration of PKC $\beta$  according to the legend.

1082



1083

1084

**Figure 4. Activating phosphorylation at the helical domain leads to opening of the regulatory motif**

1085

**A.** HDX-MS comparing apo and phosphorylated p110 $\gamma$ . Significant differences in deuterium exchange are mapped on to the structure and cartoon of p110 $\gamma$  according to the legend (PDB: 7MEZ).

1086

1087

**B.** The graph of the #D difference in deuterium incorporation for p110 $\gamma$ , with each point representing a single peptide. Peptides colored in red are those that had a significant change in the mutants (greater than 0.4 Da and 5% difference at any timepoint, with a two tailed t-test  $p < 0.01$ ). Error bars are S.D. ( $n=3$ ).

1088

1089

**C.** Representative bimodal distribution (EX1 kinetics) observed in the helical domain peptides of p110 $\gamma$ .

1090

1091

**D.** Representative p100 $\gamma$  peptides displaying increases in exchange in the phosphorylated state are shown.

1092

For all panels, error bars show SD ( $n=3$ )

1093

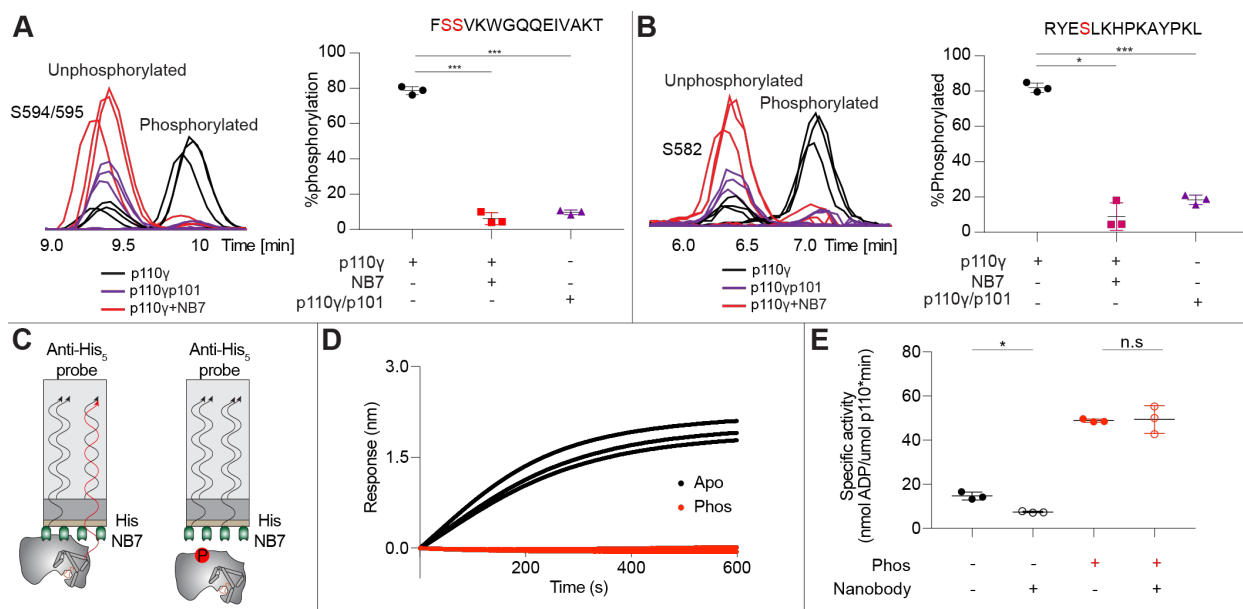
1094

**E.** Lipid kinase activity assays of phosphorylated and non-phosphorylated p100 $\gamma$  (concentration, 12nM to 1000nM) ATPase activity (left) and membrane (5% phosphatidylinositol 4,5-bisphosphate (PIP2), 95% phosphatidylserine (PS)) activation (right). Significance is indicated by \*\* (<0.001%), and \*\*\* (<0.0001%).

1095

1096

1097



1098

1099 **Figure 5. Nanobody NB7 blocks PKC phosphorylation, and phosphorylation prevents nanobody**  
 1100 **binding.**

1101 **A.** Graph showing the intensities of phosphorylated and non-phosphorylated p110γ peptide (593-607) for  
 1102 PKC (500 nM) treated p110γ (black), PKC treated p110γ with NB7 (red) and PKC treated p110γp101  
 1103 (purple). Scatter plot showing the percent phosphorylation of each complex from the left graph for the  
 1104 indicated peptide (n=3, right). Significance is indicated by \*\*\*(<0.0001%).

1105 **B.** Graph showing the intensities of phosphorylated and non-phosphorylated p110γ peptide (579-592) for  
 1106 PKC treated p110γ (black), PKC treated p110γ with NB7 (red) and PKC treated p110γp101 (purple).  
 1107 Scatter plot showing the percent phosphorylation of each complex from the left graph for the indicated  
 1108 peptide (n=3, right). Significance is indicated by \* (<0.01%), and \*\*\*(<0.0001%).

1109 **C.** Cartoon schematic of BLI analysis of the binding of immobilized His-NB7 to phosphorylated and non-  
 1110 phosphorylated p110γ.

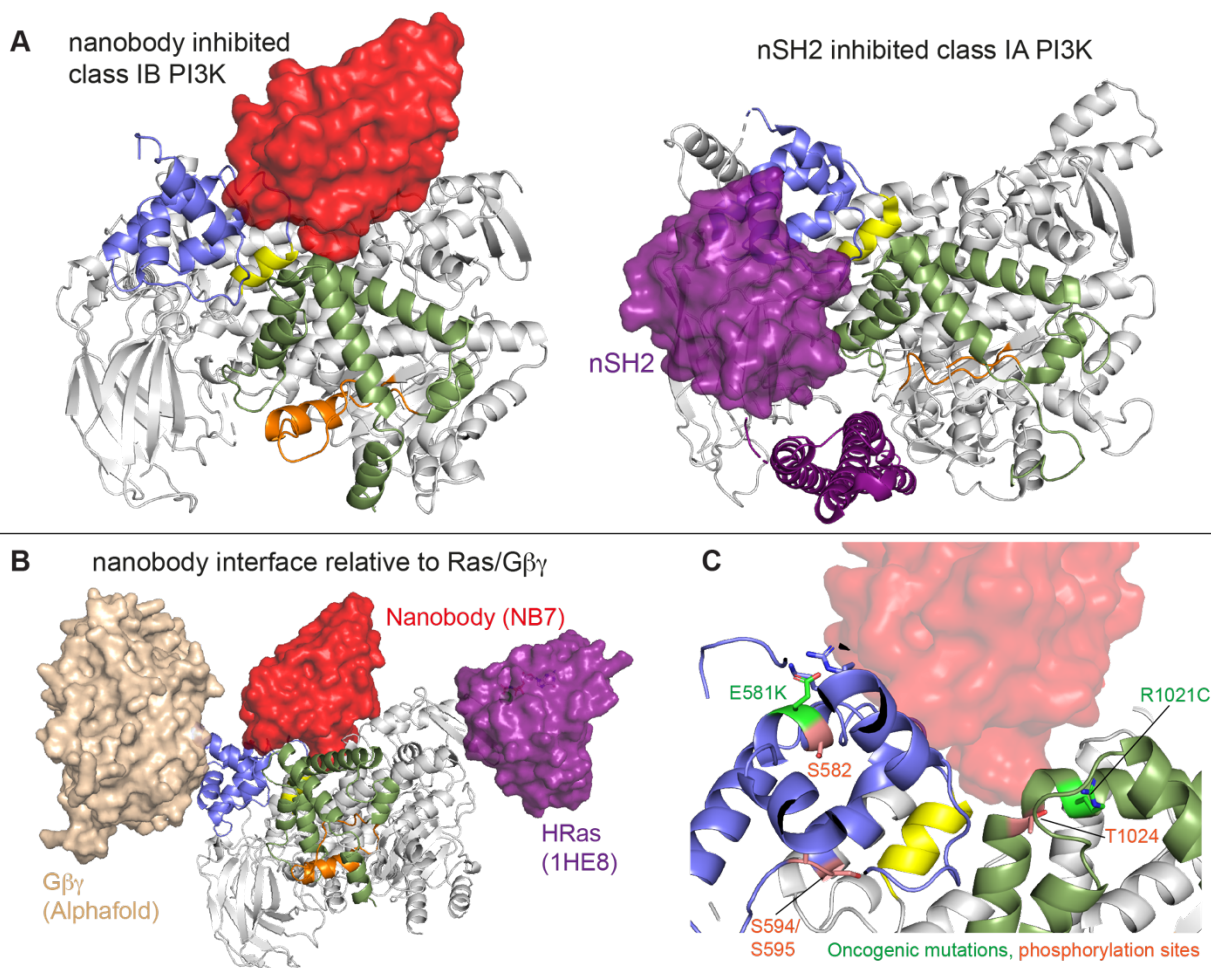
1111 **D.** Association curves for phosphorylated and non-phosphorylated p110γ (25nM) binding to His-NB7 are  
 1112 shown (n=3).

1113 **E.** Kinase activity assays comparing the activation/inhibition of phosphorylated and non-phosphorylated  
 1114 p110γ (concentration, 12nM to 1000nM) with or without nanobody (3000nM final). Significance is indicated  
 1115 by \* (<0.05%), and NS (>0.05%).

1116

1117

1118



1119

1120 **Figure 6. Comparison of nanobody binding site compared to p85 inhibition of class IA PI3Ks and**  
1121 **class IB activation sites**

1122 **A.** Comparison of the nanobody NB7 binding site in p110 $\gamma$  compared to the nSH2 inhibitory site in p110 $\alpha$   
1123 (PDB: 3HHM) (Mandelker et al., 2009)

1124 **B.** Comparison of the nanobody NB7 binding site in p110 $\gamma$  compared to the X-ray structure of the Ras  
1125 binding site (PDB: 1HE8) (Pacold et al., 2000) and the AlphaFold model of G $\beta\gamma$  bound to p110 $\gamma$   
1126 (Rathinaswamy et al., 2023).

1127 **C.** Oncogenic mutations and post-translational modifications in spatial proximity to the nanobody binding  
1128 site.

1129

1130

1131

1132  
1133  
1134  
1135  
1136  
1137  
1138  
1139  
1140  
1141  
1142  
1143  
1144  
1145  
1146  
1147  
1148  
1149  
1150  
1151  
1152  
1153  
1154  
1155  
1156  
1157  
1158  
1159  
1160  
1161  
1162  
1163

## Supplemental information for:

### **Allosteric activation or inhibition of PI3K $\gamma$ mediated through conformational changes in the p110 $\gamma$ helical domain**

Noah J Harris<sup>1\*</sup>, Meredith L Jenkins<sup>1\*</sup>, Sung-Eun Nam, Manoj K Rathinaswamy<sup>1</sup>,  
Matthew Parson<sup>1</sup>, Harish Ranga-Prasad<sup>1</sup>, Udit Dalwadi<sup>2</sup>, Brandon E Moeller<sup>1</sup>, Eleanor  
Sheekey<sup>1</sup>, Scott D Hansen<sup>3</sup>, Calvin K Yip<sup>2%</sup>, and John E Burke<sup>1,2%</sup>

<sup>1</sup>Department of Biochemistry and Microbiology, University of Victoria, Victoria, British  
Columbia, V8W 2Y2, Canada

<sup>2</sup>Department of Biochemistry and Molecular Biology, The University of British Columbia,  
Vancouver, British Columbia V6T 1Z3, Canada

<sup>3</sup>Institute of Molecular Biology, University of Oregon, Eugene, OR 97403

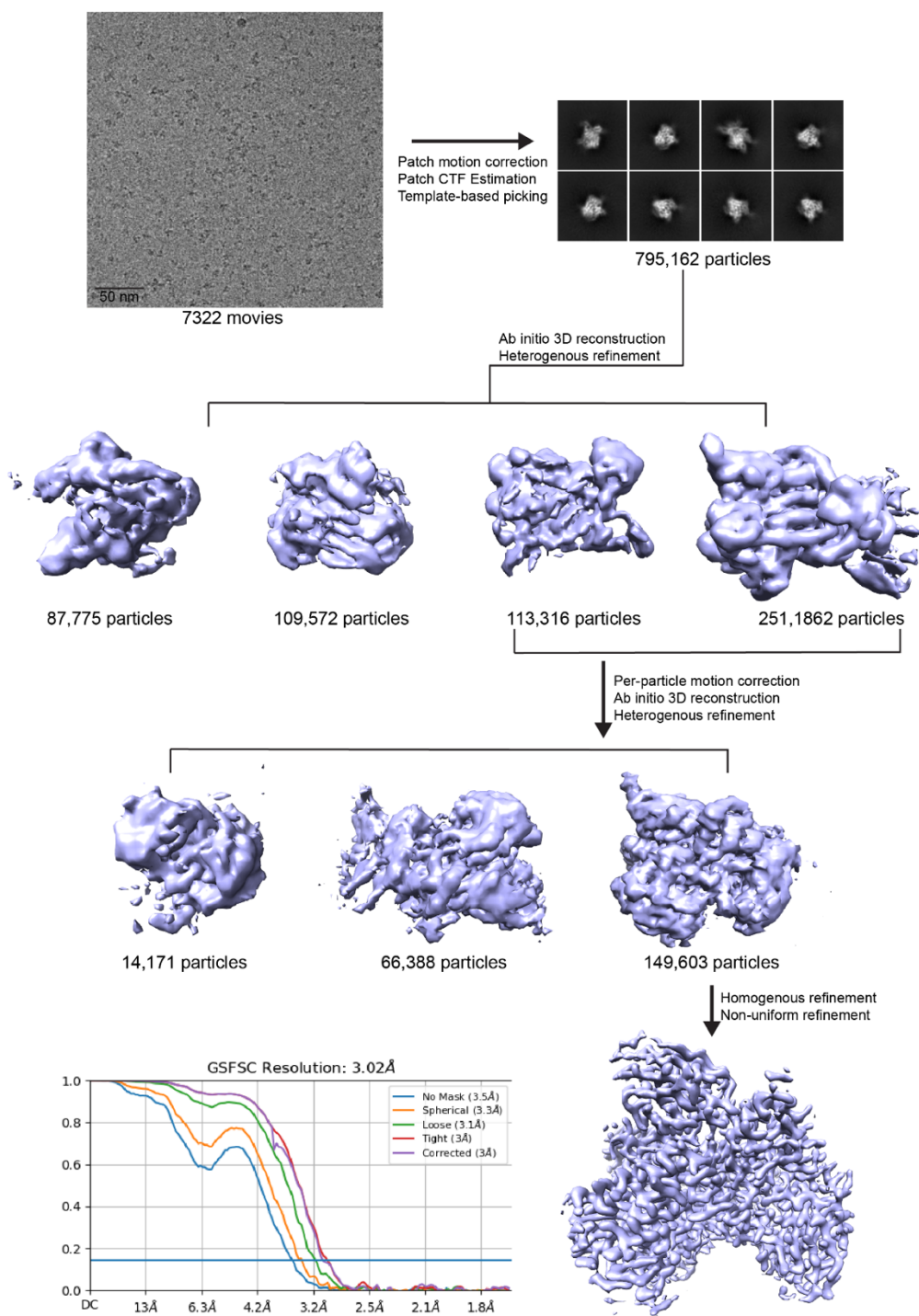
\*These authors contributed equally

%To whom correspondence should be addressed: John E. Burke

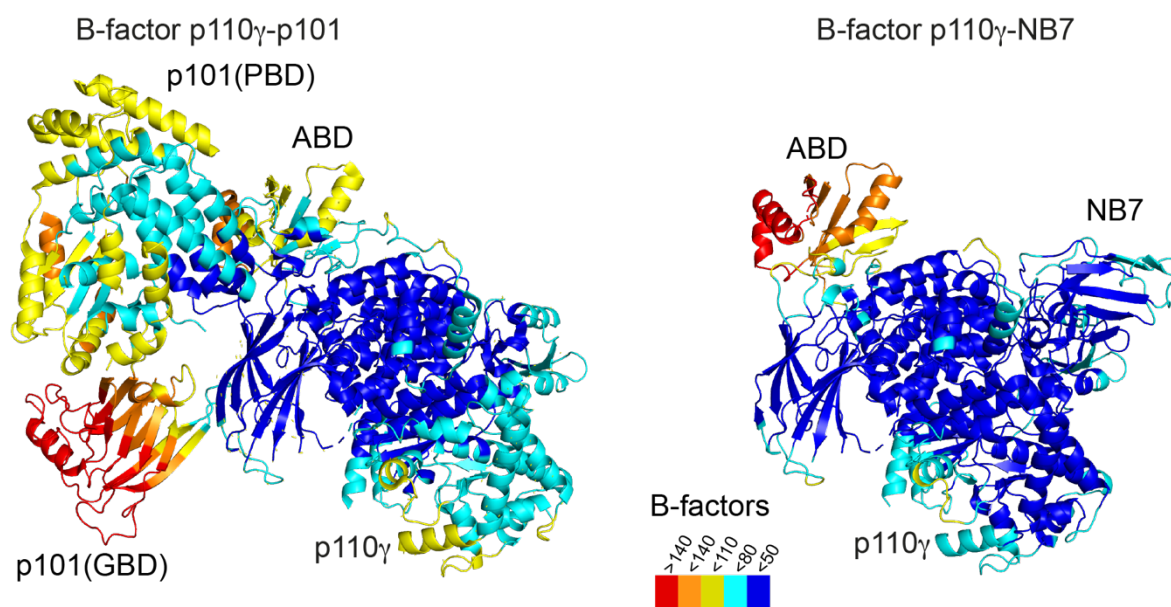
Tel: 1-250-721-8732, email: [jeburke@uvic.ca](mailto:jeburke@uvic.ca)

[Calvin K Yip](#)

[Tel: 1-604-827-3976](tel:1-604-827-3976), [em ail: calvin.yip@ubc.ca](mailto:calvin.yip@ubc.ca)



1164  
 1165 **Figure S1. p110 $\gamma$ -NB7 complex cryo-EM analysis workflow (related to main figure 2):** cryo-EM  
 1166 processing workflow of p110 $\gamma$ -NB7 complex are shown in order of a representative micrographs,  
 1167 representative 2D classification and 3D reconstruction processing strategy. Bottom left shows Gold-  
 1168 standard Fourier shell Correlation (FSC) curve of final round on non-uniform homogenous refinement.

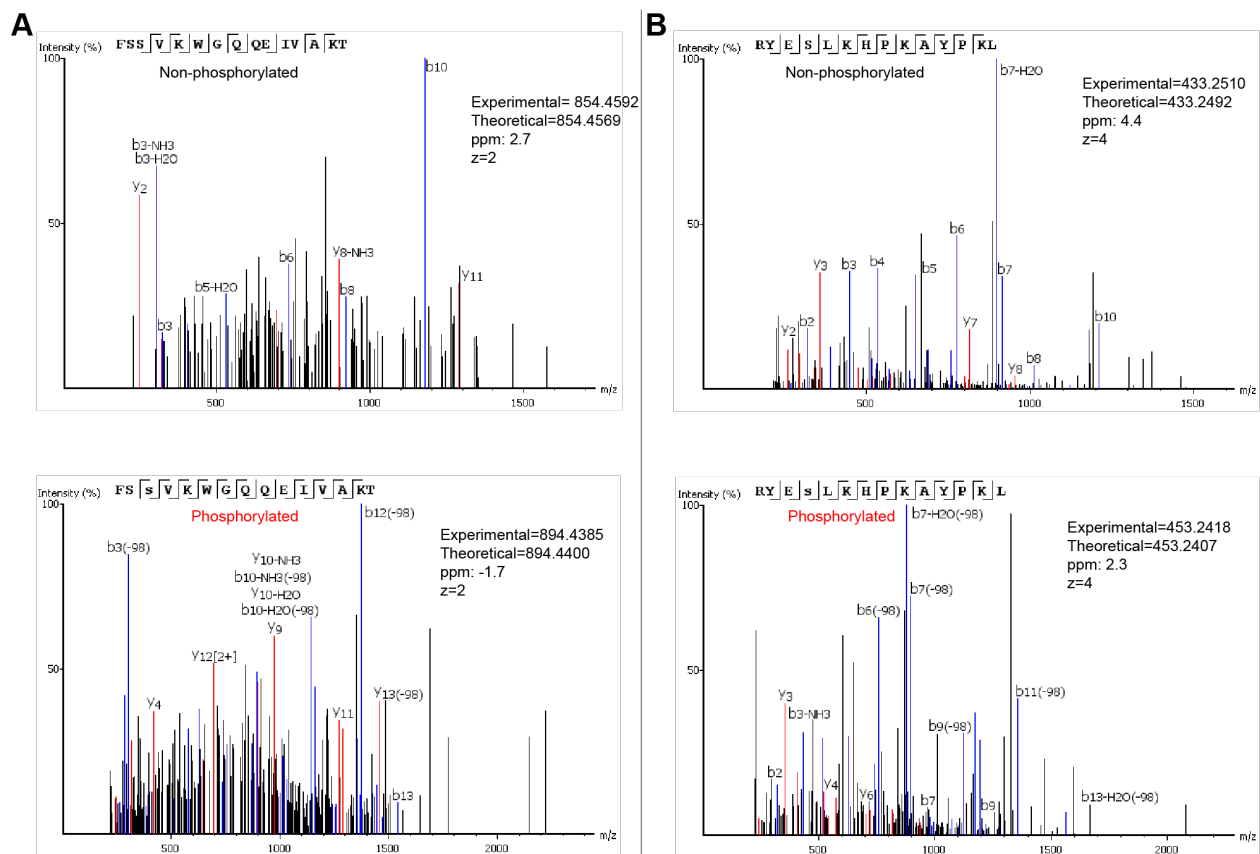


1169

1170 **Figure S2. Comparison of full length p110 $\gamma$  bound to NB7 compared to p110 $\gamma$ -p101 (related to**

1171 **main figure 2):** The structure of the p110 $\gamma$ -p101 complex (PDB:7MEZ) compared to the NB7-p110 $\gamma$

1172 complex is shown colored according to B factor based on the legend.



1173  
 1174  
 1175  
 1176  
 1177  
 1178  
 1179  
 1180  
 1181  
 1182  
 1183  
 1184  
 1185  
 1186  
 1187  
 1188  
 1189  
 1190  
 1191  
 1192  
 1193  
 1194

**Figure S3 (related to main figure 3).** MS/MS spectra of peptides spanning S582 and S594/S595 for both phosphorylated and unphosphorylated states. The theoretical and experimental mass are annotated for all peptides.

1195  
1196  
1197

**Supplementary table 1. Cryo-EM data collection, refinement and validation statistics  
(related to main figure 2)**

---

	p110 $\gamma$ -NB7
	EMD- 27627
	PDB: 8DP0
<hr/>	
<b>Data collection and processing</b>	
Magnification	
Voltage (kV)	300
Electron exposure (e/ Å <sup>2</sup> )	50
Defocus range (nM)	500-2500
Pixel size (Å)	
Symmetry imposed	C1
Initial particle images (no.)	795,162
Final particle images (no.)	149,603
Map resolution (Å)	3.02
FSC threshold	0.143
Map resolution range (Å)	2.6-4.4
<b>Refinement</b>	
Initial model used (PDB)	7MEZ (p110 $\gamma$ only)
Model Resolution (Å)	3.02
FSC threshold	0.5
Map sharpening B factor	Sharpened locally
Model composition	
Non-hydrogen atoms	8737
Protein residues	1,066
Ligands	0
<i>B</i> -factors	
Protein	52.4
Validation	
Mol probability score	1.29
Clashscore	5.33
Poor rotamers (%)	0.0
Ramachandran	
Favored	98.41
Allowed	1.59
Outliers	0.0
R.m.s. deviations	
Bond lengths (Å)	0.002
Bond angles (°)	0.490
Model to map fit (CC_mask)	0.86

---

1198  
1199  
1200  
1201  
1202

1203  
1204  
1205  
1206

**Supplementary table 2. HDX-MS data collection and validation statistics  
(related to main figure 4)**

Data set	p110y unphosphorylated	p110y phosphorylated
HDX reaction details	%D <sub>2</sub> O=75.5% pH <sub>(read)</sub> =7.5 Temp=4°C, 20°C	%D <sub>2</sub> O=75.5% pH <sub>(read)</sub> =7.5 Temp=4°C, 20°C
HDX time course (seconds)	3s at 4°C, 3s, 30s, 300s, 3000s at 20 °C	3s at 4°C, 3s, 30s, 300s, 3000s at 20 °C
HDX controls	N/A	N/A
Back-exchange	No correction, deuterium levels are relative	No correction, deuterium levels are relative
Number of peptides	244	244
Sequence coverage	98.4%	98.4%
Average peptide /redundancy	Length= 15.2 Redundancy= 3.3	Length= 15.2 Redundancy= 3.3
Replicates	3	3
Repeatability	Average StDev=0.53%	Average StDev=0.57%
Significant differences in HDX	>5% and >0.4 Da and unpaired t-test ≤0.01	>5% and >0.4 Da and unpaired t-test ≤0.01

1207